

RHODES UNIVERSITY

MASTERS THESIS

Observations of diffuse radio emission in
the Abell 773 galaxy cluster

Author:

Gift L. Sichone

Supervisor:

Prof. Gianni Bernardi

Prof. Oleg M. Smirnov

Orcid iD number:

<http://orcid.org/000-00010-6020-8549>

*A thesis submitted in fulfillment of the requirements
for the degree of Master of Science*

in the

Centre for Radio Astronomy Techniques & Technologies
Department of Physics and Electronics

February 2020

Declaration of Authorship

I, Gift L. Sichone, declare that this thesis titled, “Observations of diffuse radio emission in the Abell 773 galaxy cluster” and the work presented in it are my own. I confirm that:

- This work was done wholly or mainly while in candidature for a research degree at this University.
- Where any part of this thesis has previously been submitted for a degree or any other qualification at this University or any other institution, this has been clearly stated.
- Where I have consulted the published work of others, this is always clearly attributed.
- Where I have quoted from the work of others, the source is always given. With the exception of such quotations, this thesis is entirely my own work.
- I have acknowledged all main sources of help.
- Where the thesis is based on work done by myself jointly with others, I have made clear exactly what was done by others and what I have contributed myself.

Signed:

Date:

“A journey of a thousand miles begins with a single step.”

A famous Chinese proverb

RHODES UNIVERSITY

Abstract

Faculty of Science
Department of Physics and Electronics

Master of Science

Observations of diffuse radio emission in the Abell 773 galaxy cluster

by Gift L. Sichone

In this thesis, we present 18 and 21 cm observations of the A 773 galaxy cluster observed with the Westerbork radio telescope. The final 18 and 21 cm images achieve a noise level of $0.018 \text{ mJy beam}^{-1}$ and $0.025 \text{ mJy beam}^{-1}$ respectively.

After subtracting the compact sources, the low resolution images show evidence of a radio halo at 18 cm, whereas its presence is more uncertain in the low resolution 21 cm images due the presence of residual sidelobes from bright sources.

In the joint analysis of both frequencies, the radio halo has a 5.37 arcmin^2 area with a 6.76 mJy flux density. Further observations and analysis are, however, required to fully characterize its properties.

Acknowledgements

I will first like to thank the Development in Africa with Radio Astronomy (DARA) project for kickstarting my journey into Radio Astronomy. I am also thankful Dr. Patrick Sibanda and Dr. Habatwa V. Mweene for encouraging me to apply as a trainee in the second cohort of the DARA - AVN Radio Astronomy training workshop of 2016 hosted between the University of Zambia and HartRAO, South Africa. The training workshop convinced me to pursue a science career in Radio Astronomy.

However, the progress I have made up to date in Radio Astronomy culminating into this Master's thesis would not have been possible without the generous bursary from South African Radio Astronomy Observatory (SARAO) to study for this degree at Rhodes University. In the same vein, I will like to extend my gratitude to the University of Zambia for granting me the required permission and time to pursue this second Master's degree.

This Masters' degree work would not have seen the day of light without my supervisor, Prof Gianni Bernardi. Despite facing severe knowledge gaps and shortcomings about Radio Astronomy, Gianni still agreed to take me under his wing and proceeded with the difficult task of making a radio astronomer out of me. He has proved himself the best teacher I have ever learned from exercising firmness, patience, and kindness in perfect balance. On several occasions when I would dig myself into a hole, he never tired but instead patiently show me where I erred and after that would give me just enough rope to dig myself out. I will eternally be thankful for the opportunity you gave me to learn at your feet.

My time at Rhodes University and in Grahamstown would not have been possible without the supportive and caring students in the RATT research group and Mrs. Ronel Groenewald (former RATT admin manager). Ulrich and Kela were especially fun to be around with, and I enjoyed every one of our Friday football matches. I also made many new friends who made my time in Grahamstown memorable. Mr. Khazike Sakala, my housemate for the past two and a half years, ranks highly, and I am grateful for the kindness he showed me during our stay together. I am also thankful to two women friends: Astridah Bridget Munsaka and Thulisa Mpofu, for cheerleading and encouraging me to push every day up to the finish line. My family back home in Zambia has played a huge supportive role mentally and emotionally by regularly checking on me to see if I was okay.

Lastly, I will like to thank Jehovah God for the breath of life, good health, and favor, which has allowed me to explore the celestial heavens and see this work to completion.

Contents

Declaration of Authorship	i
Abstract	iii
Acknowledgements	iv
Contents	v
List of Figures	vii
List of Tables	ix
Abbreviations	x
Physical Constants	xii
Symbols	xiii
1 Diffuse radio emission in galaxy clusters	1
1.1 Radio Halos	2
1.1.1 Giant Radio Halos	2
1.1.2 Radio mini-halos	7
1.2 Cluster radio shocks	8
1.3 Revived AGN fossil plasma sources	10
1.4 Abell 773	12
2 Introduction to radio interferometry	15
2.1 The two-element interferometer	16
2.2 Introduction to calibration and imaging	18
2.3 Westerbork Synthesis Radio Telescope	21
3 Observations of Abell 773 at 18 cm	23
3.1 Observations and data reduction at 18 cm	23
4 Observations of Abell 773 at 21 cm	33
4.1 Observation and data reduction at 21 cm	33

5 Observations of Abell 773 at 19.43 cm	42
5.1 Observations and data reduction at 19.43 cm	42
6 Conclusion	46
Bibliography	48

List of Figures

1.1	A radio map of prototype GRH Coma C in Coma cluster at 300 MHz . . .	3
1.2	Correlation between $P_{1.4\text{GHz}}$ and LLS	4
1.3	The distribution of galaxy clusters in the $P_{1.4\text{GHz}} - L_{500}$ plane	5
1.4	The distribution of galaxy clusters in the $P_{1.4\text{GHz}} - M_{500,\text{SZ}}$ plane	6
1.5	Image of prototypical mini-halo in the Perseus cluster at 327 MHz	7
1.6	A radio image of the prototypical cluster radio shock 1253+275 in Coma cluster at 327 MHz	9
1.7	Example radio images of a cluster radio shock and cluster double radio shock	10
1.8	Examples radio phoenixes, revived fossil source and GReET	11
1.9	Radio and X-ray images of the center of A 773 galaxy cluster	13
2.1	Transmission of celestial EM radiation through Earth's atmosphere	15
2.2	A schematic diagram of of a two-element interferometer	16
2.3	The layout of the 14 WSRT dishes	21
3.1	Example of bandpass solutions derived from 3C48 for the sub-band centered at 1.65 GHz	25
3.2	Calibrated visibility spectrum of 3C48 at 1.65 GHz	25
3.3	Calibrated visibility spectrum of 3C286 at 1.65 GHz	26
3.4	Phase behaviour of the self-calibration solutions at 1.65 GHz	26
3.5	Uniform weighted image of the A 773 field at 18 cm	27
3.6	Uniform weighted map of centre of A 773 at 18 cm	28
3.7	Low resolution 1.713 GHz radio images of centre of A 773 imaged with robust parameter $r = 0, 0.5, 0.75$ after subtracting point sources	29
3.8	Contours from $r = 0.75$ radio images overlaid on the uniform weighted image of center of A 773 cluster	31
4.1	Example of bandpass solutions derived from 3C48 for the sub-band centered at 1.41 GHz	34
4.2	Calibrated visibility amplitude of 3C48 at 1.41 GHz	35
4.3	Calibrated visibility amplitude of of 3C286 at 1.41 GHz	35
4.4	Phase behaviour of the self-calibration solutions at 1.41 GHz	36
4.5	Uniform weighted map of A 773 at 21 cm	37
4.6	Uniform weighted map of centre of A 773 at 21 cm	38
4.7	Low resolution 1.38 GHz radio images of centre of A 773 imaged with $r = 0, 0.5, 0.75$ overlaid with contours of subtracted point sources	39
4.8	Contours from $r = 0.75$ radio images overlaid on the uniform weighted image of centre of A 773 cluster	41

5.1	Uniform weighted map of A 773 at 19.34 cm	43
5.2	Diffuse radio halo at centre of A 773 cluster at 19.43 cm re-imaged with $r = 0.75$ superimposed onto high resolution radio map of centre of A 773 cluster	44

List of Tables

3.1	Summary of the 18 cm observational setup	24
3.2	Radio properties of radio halo at centre of A 773 as a function of r at 18 cm	28
3.3	Radio properties of radio halo at centre of A 773 as a function of uvrangle at $r = 0.75$	30
4.1	Summary of the 21 cm observational setup	34
4.2	Radio properties of radio halo at centre of A 773 as a function of r at 21 cm	37
4.3	Radio properties of radio halo at centre of A 773 as a function of uvrangle at $r = 0.75$ at 21 cm	40

Abbreviations

WHIM	W arm H ot I ntergalactic M edium
ICM	I ntra C luster M edium
WATs	W ide A ngle T ails
NATs	N arrow A ngle T ails
CR	C osmic R ays
GRH	G iant R adio H alo
MH	M ini H alo
AGN	A ctive G alactic N uclei
GReETs	G ently R eacc E lation T ails
GMRT	G iant M etrewave R adio T elescope
GRHS	G MRT R adio H alo S urvey
EGRHS	E xtended G MRT R adio H alo S urvey
CMB	C osmic M icrowave B ackground
SZ	S unyaev Z eldovich
SEM	S econdary E lectron M odel
PEM	P rimary E lectron M odel
LAT	L arge A rea T elescope
VLA	V ery L arge A rray
NVSS	N RAO V LA S ky S urvey
WENSS	W esterbork N orthern S ky S urvey
LoTSS	L OFAR T wo metre S ky S urvey
WSRT	W esterbork S ynthesis R adio T elescope
ASTRON	N etherlands I nstitute of R adio A stronomy
UTC	C oordinated U niversal T ime
CASA	C ommon A stronomy S oftware A pplications

RFI	R adio F requency I nterference
PSF	P oint S pread F unction
MFS	M ulti F requency S ynthesis

Physical Constants

Speed of Light $c = 2.997\,924\,58 \times 10^8 \text{ ms}^{-1}$ (exact)

Molar Mass $M_{\odot} = 1.989 \times 10^{30} \text{ kg}$ (approx.)

Jansky $1 \text{ Jy} = 10^{-26} \text{ W m}^{-2} \text{ Hz}^{-1}$

Symbols

$P_{1.4\text{GHz}}$	1.4 GHz radio power	W Hz^{-1}
t	Time	s
α	Spectral index	
L_X	Cluster X-ray luminosity	erg s^{-1}
S_ν	Spectral flux density at ν	Jy
ν	Observing frequency	Hz
LLS	largest Linear Size	Mpc
L_{500}	Cluster X-ray luminosity computed within R_{500}	erg s^{-1}
M_{500}	Cluster mass computed within R_{500}	
θ	Angular resolution	rad
λ	Wavelength	m
D	Diameter of dish telescope	m
B_{max}	Maximum baseline	km
ω	Angular frequency	rad s^{-1}
$\vec{\mathbf{b}}$	baseline vector	
τ	Geometric time delay	s
$\hat{\sigma}$	Unit vector	
ϕ	Phase	
α	Right Ascension	
δ	Declination	
p, q	Antenna element indices	
V_p, V_q	Voltages induced in antenna elements p and q	
E	Electric field	
I	Intensity	
$V(u, v)$	Complex visibility at (u, v)	

I_I	Intrinsic sky brightness distribution
\mathbf{J}	Jones matrices
H	Hermitian
E	Telescope primary beam response
G	Gain
I_D	“dirty” image
PSF	Point Spread Function
B	Fourier transform of PSF
\otimes	Convolution
γ	Loop gain
f_{max}	Peak flux
r	Briggs robust parameter

Dedicated to my late parents Charity Musangu Mutti and Saddock Sichone, my late young brother Emmanuel Kabalwa Nakanda and late aunty Fridah Mutti. You were the best family I could ever have wished for and I miss you every day. May your souls continue to rest in peace...

Chapter 1

Diffuse radio emission in galaxy clusters

Galaxy clusters are the largest gravitationally bound structures in our Universe with typical masses of $\sim 10^{14} - 10^{15} M_{\odot}$ within 1.5 Mpc radius of the cluster centre. They are located at the intersections of the filamentary structure of the cosmic web and can contain up to several thousand galaxies that account for a small fraction (3 – 5%) of the total cluster mass. Most of the cluster mass ($\sim 80\%$) is in the form of dark matter. The remaining 15 – 17% is baryonic matter in the form of hot ($10^7 - 10^8$ K), dilute ($\sim 10^{-3}$ particles cm^{-3}) diffuse magnetized plasma held together by gravity and permeating the space between the galaxies commonly referred to as intracluster medium (ICM, e.g., [Bahcall, 1996](#), [Blumenthal et al., 1984](#), [Sarazin, 1986](#)). X-ray observations reveal that the ICM emits thermal bremsstrahlung emission from hot electrons ([Sarazin, 1986](#)). Galaxy clusters are formed via mergers and accretion of smaller structures driven by gravity. Cluster mergers are some of the most energetic events in our Universe and can release up to $\sim 10^{64}$ erg over a timescale of a few Gyrs ([Sarazin, 2002](#)). Depending on their dynamical status, galaxy clusters can be classified as relaxed or merging clusters ([Feretti et al., 2012](#)).

In the past two decades, low-frequency radio observations of an increasing number of galaxy clusters have revealed the presence of diffuse, Mpc-size radio sources of synchrotron origin. These sources are associated with cosmic-ray (CR) electrons and large-scale magnetic fields of the order of $\sim 0.1 - 1 \mu\text{G}$ mixed with the thermal ICM gas. Historically, these diffuse, extended radio sources were classified into three main types: radio halos, radio relics, and mini-halos ([Brunetti & Jones, 2014](#), [Feretti & Giovannini, 1996](#), [Feretti et al., 2012](#)).

Recently, [van Weeren et al. \(2019\)](#) proposed reclassifying these diffuse, large-scale radio sources inside galaxy clusters associated with the ICM into three broad groups: radio halos, cluster radio shocks and revived active galactic nuclei (AGN) fossil plasma sources. The radio halo class now includes giant radio halos (GRHs), mini-halos (MHs) and possibly "hybrid" or "intermediate" radio halos (i.e., radio halos whose properties fall in between those of GRHs and MHs).

1.1 Radio Halos

1.1.1 Giant Radio Halos

GRHs are diffuse, Mpc-size radio sources of synchrotron origin frequently detected at the centre of a fraction of massive and merging galaxy clusters. GRHs are typically extended with linear sizes in the range of 1–2 Mpc. They generally show smooth, regular morphologies that approximately follow the shape of the hot X-ray gas from the ICM ([Bonafede et al., 2015](#), [Botteon et al., 2018](#), [Cuciti et al., 2018](#), [de Gasperin et al., 2015](#), [Sommer et al., 2016](#), [Van Weeren et al., 2013](#), [Venturi et al., 2017](#)). In a few exceptional cases, GRHs have been found to show irregular morphologies (e.g., A 665; [Giovannini & Feretti, 2000](#)). At 1.4 GHz, GRHs are unpolarized, typically show $\sim 0.1 - 1 \mu\text{Jy arcsec}^{-2}$ surface brightness and radio power ($P_{1.4\text{GHz}}$) in the $\sim 10^{24} - 10^{25} \text{ W Hz}^{-1}$ range. They are characterised by steep spectra with spectral index values: $\alpha = 1.1 - 1.4$ ¹ ([Brunetti & Jones, 2014](#), [Feretti, 2002](#), [Feretti et al., 2012](#), [Giovannini & Feretti, 2002](#), [Govoni et al., 2001](#), [van Weeren et al., 2019](#)). The advent of highly sensitive, very low frequency radio observations of galaxy clusters has revealed the existence of a subclass of GRHs referred to as ultra-steep spectrum radio halos (USSRHs). These radio sources are characterized by very steep spectra (up to $\alpha \sim 2$) and are missed by GHz observations ([Feretti et al., 2012](#), [van Weeren et al., 2019](#), [Wilber et al., 2017](#)). Figure 1.1 shows the prototypical GRH source Coma C located at the centre of the Coma cluster ([Feretti et al., 2012](#), [Giovannini et al., 1993](#)).

GRHs are not a common property of galaxy clusters. At present, there are 65 confirmed GRHs from literature, all being found in massive and merging clusters ([van Weeren et al., 2019](#)). A survey of 64 X-ray luminous ($L_X \gtrsim 5 \times 10^{44} \text{ erg s}^{-1}$) galaxy clusters carried out with the Giant Metrewave Radio Telescope (GMRT) at 235 and 610 MHz ([Kale et al., 2015, 2013](#), [Venturi et al., 2009, 2008](#)) showed that GRHs are hosted in only $\sim 20 - 30\%$ of the sample. [Cassano et al. \(2008\)](#) showed that the fraction of galaxy clusters hosting GRHs increases with the cluster X-ray luminosity.

¹with $S_\nu \propto \nu^{-\alpha}$, where S_ν is the flux density and ν the observing frequency

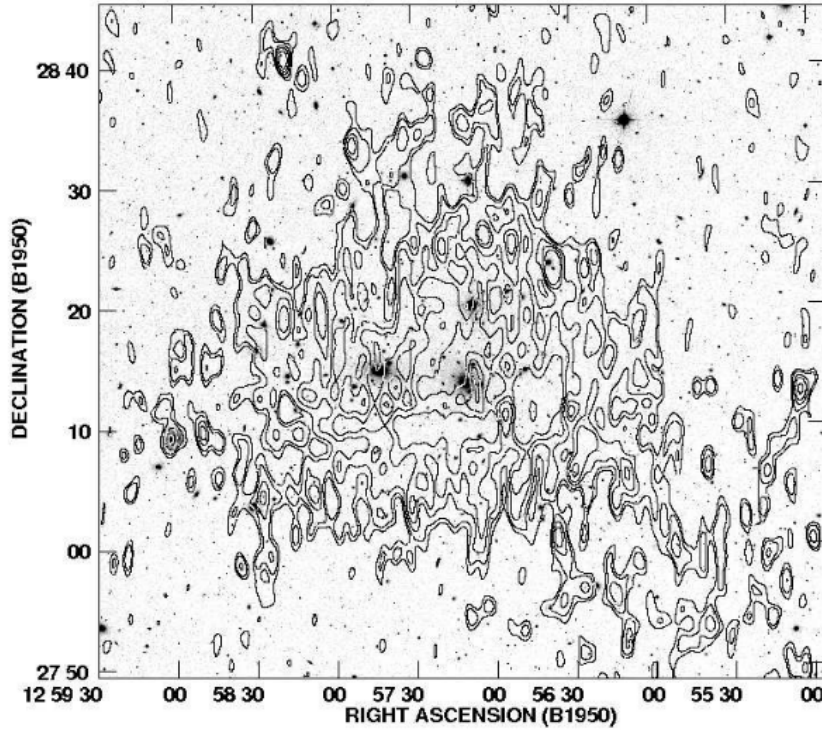


FIGURE 1.1: Contours of the GRH source Coma C in the Coma cluster at 300 MHz, superimposed on the Digital Sky Survey optical image (Feretti et al., 2012). Contour levels are drawn at 3, 6, 12, 25, 50, 100 mJy beam⁻¹.

Giovannini et al. (2009) found a linear correlation between the 1.4 GHz radio power of GRHs $P_{1.4\text{GHz}}$ and its largest linear size (LLS, Figure 1.2). More recently, correlations were found between $P_{1.4\text{GHz}}$ and the cluster X-ray luminosity measured within R_{500} ² ($L_{500} > 5 \times 10^{44}$ ergs s⁻¹, Brunetti et al., 2009, Cassano et al., 2013, Giovannini et al., 2009), temperature (Liang et al., 2000) and mass (e.g., Bernardi et al., 2015), indicating a cluster bimodal distribution. The correlation between $P_{1.4\text{GHz}}$ and L_{500} shown in galaxy clusters hosting GRHs trace the $P_{1.4\text{GHz}} - L_{500}$ correlation, while galaxy clusters without GRHs lie below the correlation (Brunetti et al., 2009, Cassano et al., 2013).

With the advent of sensitive, arcminute-resolution Cosmic Microwave Background (CMB) telescopes, it has been possible to use the Sunyaev-Zel'dovich (SZ) effect to detect galaxy clusters and measure their masses (Ade et al., 2011, Birkinshaw, 1999, Ruhl et al., 2004, Sunyaev & Zel'Dovich, 1980). Several authors found a correlation between $P_{1.4\text{GHz}}$ and the SZ cluster mass $M_{500,\text{SZ}}$ ³, $P_{1.4\text{GHz}} \propto M_{500,\text{SZ}}^{\alpha_c}$, with $3 < \alpha_c < 4$ (e.g., Basu, 2012, Bernardi et al., 2015, Cassano et al., 2013, Figure 1.4).

²where R_{500} is radius corresponding to a total density contrast $500\rho_c(z)$, where $\rho_c(z)$ is the critical density of the Universe at the cluster redshift

³where $M_{500,\text{SZ}}$ is the total cluster mass within the radius R_{500}

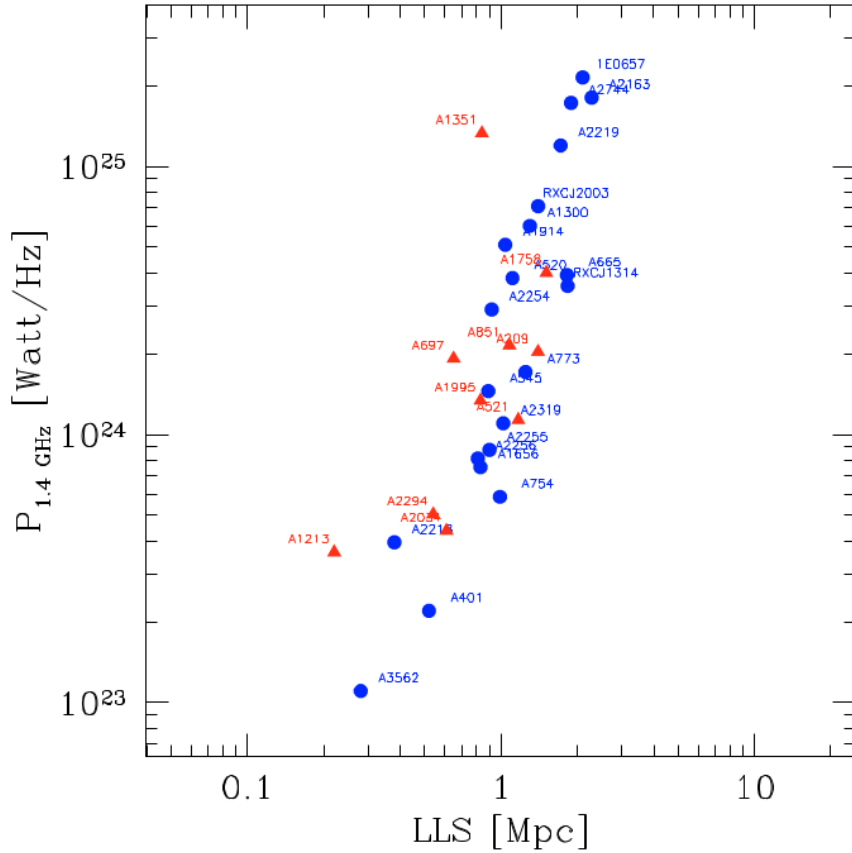


FIGURE 1.2: Correlation between 1.4 GHz radio halo power of GRHs, $P_{1.4\text{GHz}}$, and their largest linear size, LLS (Giovannini et al., 2009). Red triangles are new radio halos discovered by (Giovannini et al., 2009) while blue circles are previously known radio halos. This correlation suggests that giant and smaller size radio halos may have a common origin and similar physical properties.

This link between radio power and cluster merger history provides the current best way to discriminate between models of formation of GRHs. CR electrons diffusing over Mpc-scales experience radiative losses on time scales shorter than the cluster crossing time, requiring some mechanism of particle reacceleration. Two main classes of models have been proposed to explain the origin of these CR electrons. These are referred to as the Secondary Electron (or hadronic) Model (SEM, Blasi & Colafrancesco, 1999, Dennison, 1980, Enßlin et al., 2011, Pfrommer & Ensslin, 2004b) and the Primary Electron (or turbulent re-acceleration) Model (PEM, Beresnyak et al., 2013, Brunetti & Jones, 2014, Brunetti & Lazarian, 2011, Brunetti et al., 2001, Petrosian, 2001).

In the SEM, CR protons accumulate inside the cluster volume due to their long lifetimes and the large size of clusters, after being injected by accretion shocks and galaxy outflows from AGNs. These trapped CR protons undergo hadronic interactions with ICM protons which continuously generate secondary (or decay) products such as CR electrons, pions and neutrinos. The decay of secondary neutral pions (or π^0) into γ -ray photons is expected and is indicative of the presence of CR protons in galaxy clusters. The

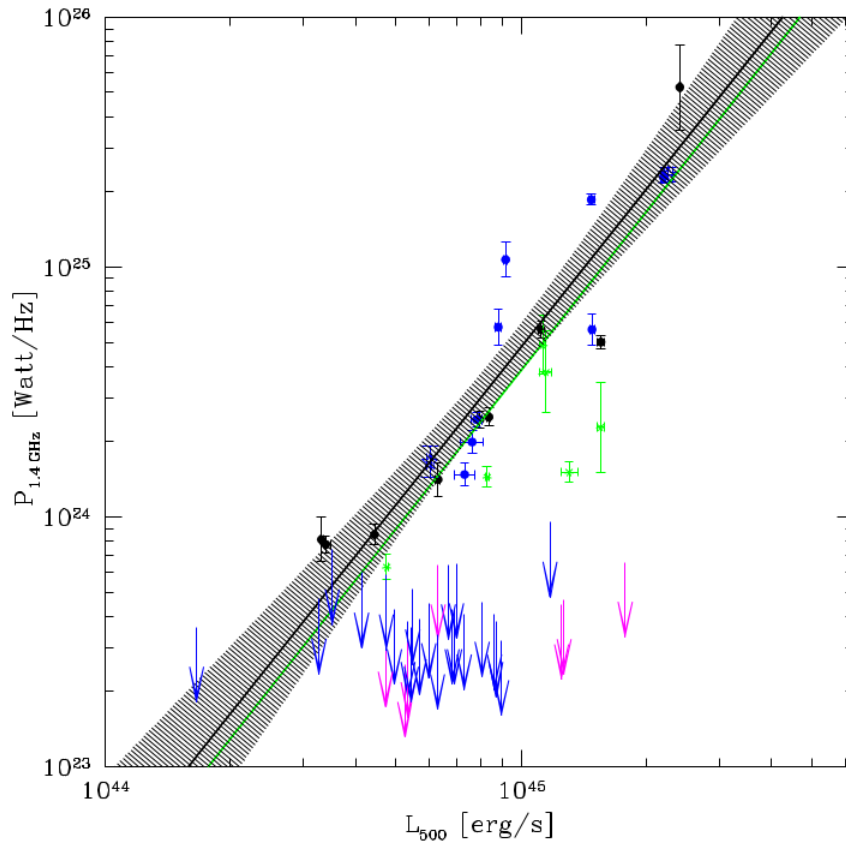


FIGURE 1.3: The distribution of galaxy clusters in the $P_{1.4\text{GHz}} - L_X$ plane (Cassano et al., 2013). Black filled dots denote GRHs from literature, blue filled dots are GRHs from the Extended-GMRT Radio Halo Survey (EGRHS, Venturi et al., 2008) sample and green asterisks represent USSRHs. The black solid line indicates the best fit line for GRHs only while the green solid line is the best fit line includes the USSRHs too. The magenta arrows are cool-core galaxy clusters belonging to the EGRHS sample. Blue arrows represent the upper limits on GHRs. There is a noticeable bimodality as most of the low luminosity systems do not host GHRs, whereas systems with GRHs followed a well defined correlation.

secondary CR electrons are expected to emit synchrotron emission in the radio regime when they interact with Mpc-sized cluster magnetic fields (e.g., Blasi & Colafrancesco, 1999, Blasi et al., 2007, Brunetti & Jones, 2014, Dennison, 1980, Keshet & Loeb, 2010, Pfrommer & Ensslin, 2004b, Pfrommer et al., 2008).

In the PEM, seeds of CR electrons are injected into the ICM from AGNs and are in-situ reaccelerated to relativistic energies by turbulence induced by cluster mergers. In presence of cluster-wide magnetic fields, they emit synchrotron radiation (e.g., Beresnyak et al., 2013, Brunetti & Lazarian, 2011, 2016, Brunetti et al., 2001, Donnert et al., 2013, Petrosian, 2001).

At present, the non detection of γ -ray emission in galaxy clusters from the orbiting Fermi Large Area Telescope (Fermi-LAT, Atwood et al., 2009) disfavors a purely hadronic origin of GRHs (Ackermann et al., 2014, Aharonian et al., 2009, Liang et al., 2016,

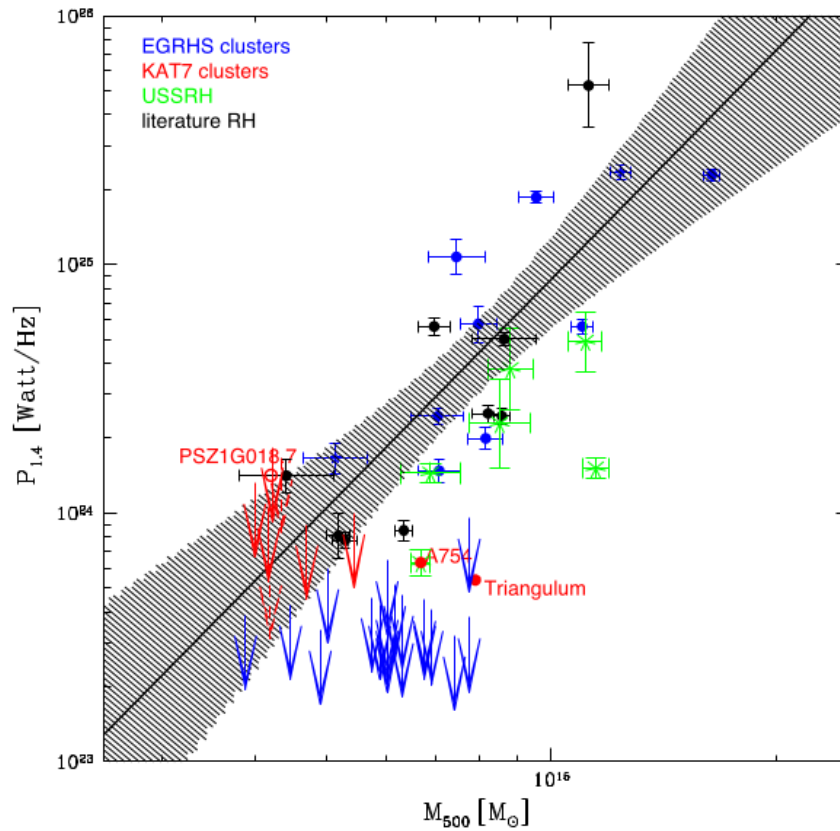


FIGURE 1.4: The distribution of galaxy clusters in the $P_{1.4\text{GHz}} - M_{500,\text{SZ}}$ plane (Bernardi et al., 2015). Blue dots represent GRHs from the EGRHS sample while black dots are GRHs already known in the literature. Arrows are upper limits (see Bernardi et al., 2015, for details). The black solid line is the best fit for GRHs and the shaded region is the 95% confidence region. Green asterisks are USSRHs.

Reimer & Sreekumar, 2004, Zandanel & Ando, 2014). Furthermore, a purely hadronic origin of GRHs has been shown to require values of cluster magnetic fields which are in tension with estimates from studies based on Faraday rotation measures (Bonafede et al., 2010, Brunetti et al., 2012, Govoni & Feretti, 2004). Nonetheless, Fermi-LAT γ -ray observations of galaxy clusters are useful for placing constraints on the CR proton content of clusters, testing the hadronic nature of GRHs and testing the contributions of secondary CR electrons in the PEM (Aharonian et al., 2009, Zandanel & Ando, 2014).

The most relevant questions that still need to be addressed are related to the origin of the reaccelerated electrons and large-scale magnetic fields. Are electrons coming from hadronic interactions or from AGN outflows? Are magnetic fields primordial or not? These will be the fundamental questions addressed by future radio surveys of galaxy clusters.

1.1.2 Radio mini-halos

Mini-halos (MHs) are diffuse, a few hundred kpc-size synchrotron radio sources found surrounding powerful radio galaxies in a fraction of relaxed galaxy clusters with cool cores (Giacintucci et al., 2014, 2017, 2013, Gitti et al., 2004, Govoni et al., 2009, Kale et al., 2015). Figure 1.5 shows the prototypical MH located in the Perseus cluster (Sijbring, 1993).

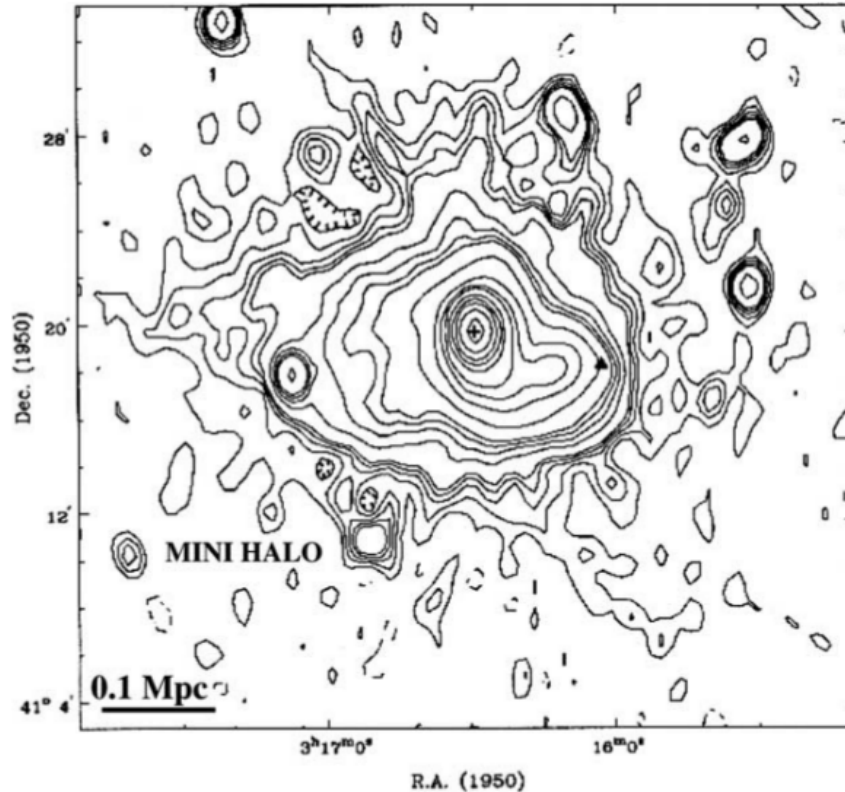


FIGURE 1.5: Image of the prototypical mini-halo in the Perseus cluster at 327 MHz. The contour levels are drawn at $-4, 4, 8, 12, 16, 20, 40, 60, 80, 100, 200, 400, 600, 800, 1500, 2500, 4000, 8000, 16000$ mJy beam^{-1} . The cross indicates the position of NGC 1275 and the triangle indicates the position of NGC 1272 (Sijbring, 1993).

At present, there are 24 known MHs. They are detected in a high fraction ($\sim 50 - 80\%$) of cool core galaxy clusters (Giacintucci et al., 2017, Kale et al., 2015, 2013, van Weeren et al., 2019). Unlike GRHs, the $P_{1.4\text{GHz}}$ of MHs shows no correlation with cluster mass, $M_{500,\text{SZ}}$, indicating that cluster mergers do not play a crucial role in their formation (Giacintucci et al., 2013).

Like the GRH case, the short lifetimes of CR electrons compared to the long diffusion times required to cross the typical MH size requires a form of reacceleration to explain the formation of MHs. Similar to GRHs, the SEM and PEM have been proposed to explain radio emission in MHs (Gitti et al., 2012, Pfrommer & Ensslin, 2004a)

The MH SEM suggests that CR electrons and γ -rays are generated from hadronic collisions between ICM protons and CR protons most likely injected from the AGN at the central radio galaxy (Keshet & Loeb, 2010, Pfrommer & Ensslin, 2004a, Zandanel & Ando, 2014). Due to their long lifetimes, CR protons can diffuse across the cluster cool core region and generate secondary CR electrons, which in turn can create the observed MH radio emission (Brunetti & Jones, 2014). However, the current non detection of clusterwide γ -rays in relaxed clusters from Fermi-LAT telescope observations disfavours a purely hadronic origin of MHs (Ackermann et al., 2014, Anderson et al., 2016, Prokhorov & Churazov, 2014). At the same time, γ -rays observations of the Perseus cluster have not completely ruled out the hadronic origin of MHs but instead impose strict upper limits on the role of hadronic interactions in the formation of MHs in relaxed clusters (Ahnen et al., 2016, Aleksić et al., 2012, 2010).

The MH PEM suggests that seeds of CR electrons in the ICM are reaccelerated to relativistic energies via turbulence in cluster cool core regions. Buoyant bubbles of plasma are inflated by the AGN and disrupted by turbulent motion of gas in the cool core (Brunetti & Jones, 2014, Cassano et al., 2008, Gitti et al., 2002). This turbulence, generated by gas sloshing, reaccelerates and spatially redistributes seeds of CR electrons to the cluster cool core regions (Mazzotta & Giacintucci, 2008, ZuHone et al., 2012). At the moment, γ -ray observations by Fermi-LAT are not deep enough to place strong constraints on the origin of MHs (Ackermann et al., 2014, Aharonian et al., 2009, Han et al., 2012).

1.2 Cluster radio shocks

Cluster radio shocks are diffuse, Mpc-size synchrotron radio sources often found at the periphery of a small fraction of massive and merging galaxy clusters. They are associated with cluster shock regions. At 1.4 GHz, they typically show a $\sim \mu\text{Jy arcsec}^{-2}$ surface brightness and elongated, arc-like shapes nearly perpendicular to the cluster radius, with sizes ranging from 500 kpc up to 2 Mpc (Lindner et al., 2014, Loi et al., 2017, Shimwell et al., 2015, Van Weeren et al., 2011, 2016). Some merging clusters host cluster double radio shocks, located on the opposite sides with respect to the cluster centre (Bagchi et al., 2011, de Gasperin et al., 2015, 2014, Röttgering et al., 1997, van Weeren et al., 2011). High resolution observations of cluster radio shocks reveal a significant amount of filamentary structure whose nature is still uncertain (Di Gennaro et al., 2018, Rajpurohit et al., 2018). Unlike GRHs, they show strongly polarized radio emission with polarization fractions up to $\gtrsim 20\%$. Cluster radio shocks are characterized by steep spectra with spectral index α in the 1.0 – 1.5 range (van Weeren et al., 2019). Figure 1.6 shows the

prototypical cluster radio shock example 1253+275 in the Coma cluster (Giovannini & Feretti, 2002, Giovannini et al., 1991). Figure 1.7 shows example of a cluster radio shock and a cluster double radio shock, respectively. Only 5% of clusters host cluster radio shocks (Kale et al., 2015, 2013).

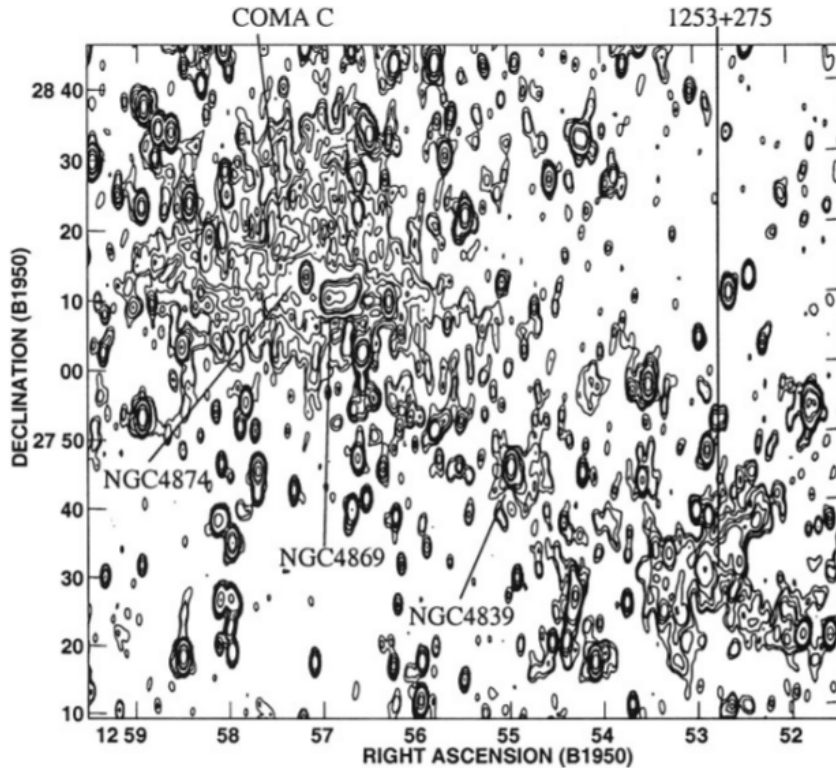


FIGURE 1.6: Radio image of the prototypical radio shock 1253+275 in the outskirts of Coma cluster at 327 MHz (Giovannini & Feretti, 2002). Contour levels are drawn at 3, 5, 7, 10, 12, 15, 20, 30, 50 mJy beam^{-1} . The cluster centre is ~ 1.2 Mpc away in the north-east direction.

Like GRHs, the cluster radio shock power $P_{1.4\text{ GHz}}$ correlates with the cluster X-ray luminosity (Feretti et al., 2012) and SZ cluster mass following a power-law relation $P_{1.4\text{ GHz}} \propto M_{500,\text{SZ}}^{\alpha_r}$, with $\alpha_r = 2.83 \pm 0.39$ (de Gasperin et al., 2014). Another correlation is found between the cluster radio shock linear size and the distance from the cluster centre, indicating that larger cluster radio shocks prefer being located in the outskirts of massive and merging clusters (Bonafede et al., 2012).

The elongated, arc-like shapes of cluster radio shocks in the cluster periphery, coupled with the short lifetimes of CR electrons, suggests that they trace CR electrons accelerated at Mpc-scales by shock waves. These ICM shock waves are grouped into two main classes: merger shocks and accretion shocks. Merger shocks are generated during mergers of subclusters (Bykov et al., 2008), while accretion shocks are derived from accretions of the warm hot intergalactic medium from the surrounding filaments of the

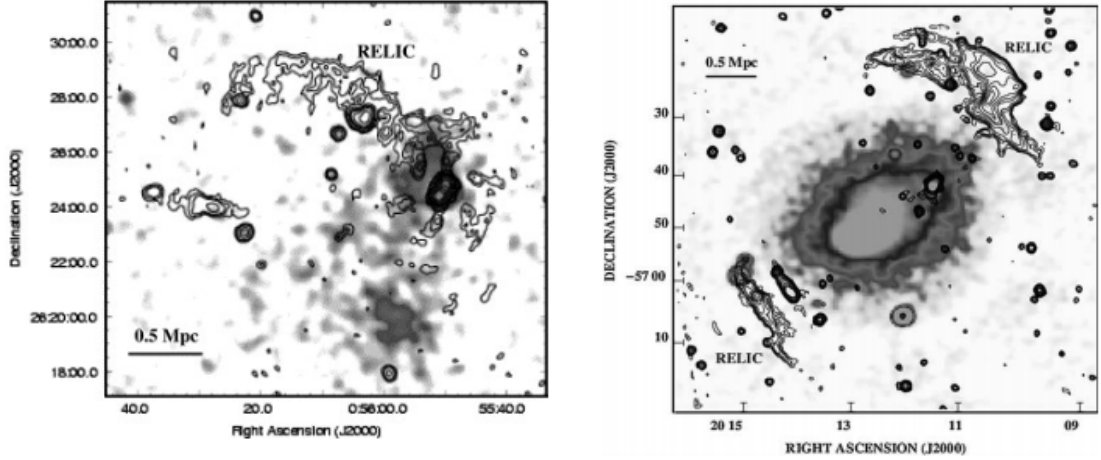


FIGURE 1.7: *Left panel:* A radio image of the radio shock in the A 115 cluster at 1.4 GHz (Feretti, 2005). *Right panel:* A radio image of the double radio shock in A 3667 cluster at 833 MHz (Feretti, 2005).

cosmic web (Brunetti & Jones, 2014). In an idealized merger, equatorial shocks form first and move outwards in the equatorial plane. After the dark matter core passage, two merger shock waves start from the cluster centre and launch in opposite directions along the merger axis (van Weeren et al., 2019, 2011). Accretion shocks are typically stronger than merger shocks, but dissipate less energy since they formed in colder, lower gas density regions far away from the cluster centre (Brunetti & Jones, 2014).

1.3 Revived AGN fossil plasma sources

Revived AGN fossil plasma sources are diffuse, kpc-size radio sources of synchrotron origin associated with fossil plasma originally from a dying or extinct AGN that has somehow been revived by shock waves or weak cluster merger-induced turbulence. The fossil plasma traces past AGN activity and could be a possible source of pre-existing CR electrons required to form radio halos and cluster radio shocks. These sources are generally located near the cluster centre, have sizes smaller than 300 – 400 kpc and typically show $P_{1.4\text{GHz}} < 10^{24} \text{ W Hz}^{-1}$ (Cohen & Clarke, 2011, de Gasperin et al., 2015, Mandal et al., 2019, Slee et al., 2001, van Weeren et al., 2011). Most revived AGN fossil plasma sources have roundish and filamentary shapes and exhibit extremely steep spectra with an mean spectral index $\alpha \sim 2$ (Feretti et al., 2012). In most cases, their spectra is curved and shows high frequency steepening. They also show polarized radio emission with polarization fraction $\lesssim 20\%$ (Kempner et al., 2004, Mandal et al., 2019).

Revived AGN fossil plasma sources as shown in Figure 1.8 now include radio phoenixes (de Gasperin et al., 2015), revived fossil sources (formerly AGN relics, Kempner et al.,

2004, Mandal et al., 2019) and the recently discovered Gently Re-accelerated Tails (GReETs, de Gasperin et al., 2017). Radio phoenixes trace old radio plasma from previous AGN activity which is no longer visible due to synchrotron losses. When a merger shock or accretion shock wave passes through this old plasma, it is compressed together with cluster magnetic fields, leading to re-acceleration of fossil CR electrons to mild ($\gamma \sim 100$) relativistic energies. The fossil plasma once again becomes visible in the radio regime (de Gasperin et al., 2015, Kempner et al., 2004).

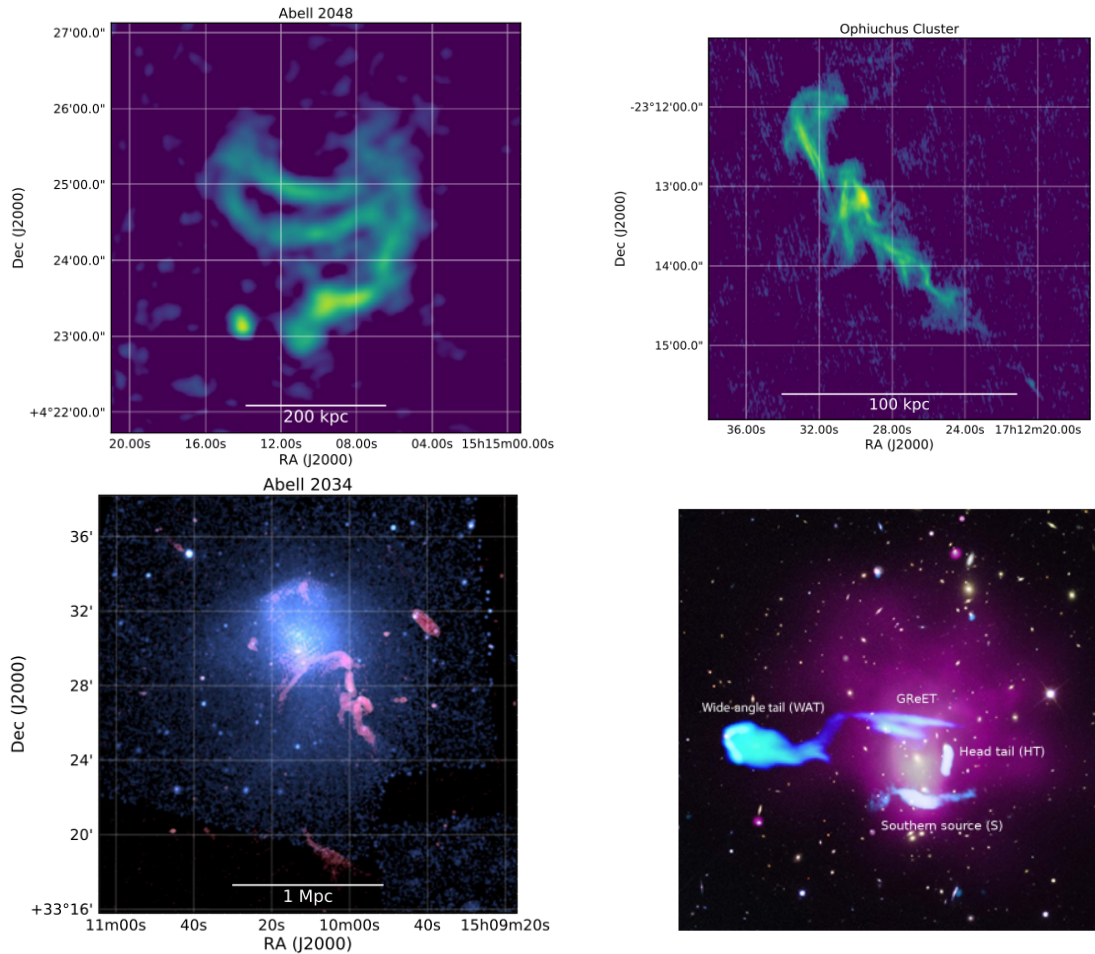


FIGURE 1.8: Examples radio phoenixes, revived fossil source and GReET. *Top left panel:* A GMRT radio image of a radio phoenix in the A 2048 cluster at 325 MHz. *Top right panel:* A VLA radio image of the elongated radio phoenix in Ophiuchus cluster at 1.4 GHz. *Bottom left panel:* LOFAR 118 – 166 MHz (red) and Chandra 0.5 – 2.0 keV (blue) composite image of the revived fossil source in A 2034 (van Weeren et al., 2019). *Bottom right panel:* Composite image showing optical background from Sloan Digital Sky Survey (SDSS), LOFAR (blue) and Chandra 0.5–4 keV (purple) emission of the GReET in A 1033 (de Gasperin et al., 2017).

Revived fossil sources are associated with radio galaxies whose AGN has switched off. As the source ages, it loses energy through synchrotron and inverse Compton losses and

eventually appears as an X-ray cavity with no observable radio emission at \sim GHz frequencies. When a merger or accretion shock makes contact with these radio lobes or cocoons, they first adiabatically compress the plasma and tear these cocoons into filamentary radio structures (Ensslin, 2001, Ensslin & Brueggen, 2002). Observational examples of revived fossil sources are found in A 2034 (Shimwell et al., 2016), A 1132 (Wilber et al., 2017), A 1913 (Brüggen et al., 2018), VLSS J1431.8+1331, VLSS J1133.7+2324 and VLSS J1117.1+7003 (van Weeren et al., 2011). GReETs, on the other hand, are radio galaxy tails that are somehow revived after fading due to radiative losses. Their radiative losses are just barely balanced by particle re-acceleration mechanisms such as turbulence and shocks (de Gasperin et al., 2017).

At present, there are 13 confirmed revived AGN fossil plasma sources revealed through low-frequency observations. However, their precise origin remains uncertain because they remain undetected at GHz frequencies, due to their steep spectra. Some of these sources (e.g., in A 85, A 1664 and A 4038) have been found in relaxed galaxy clusters, indicating that major merger events are not required for their formation (van Weeren et al., 2019).

1.4 Abell 773

Abell 773 (A 773 hereafter) is a rich galaxy cluster at redshift $z = 0.217$, located at R.A. = $09^{\text{h}}17^{\text{m}}52.8^{\text{s}}$, Dec. = $51^{\text{d}}43^{\text{m}}48.0^{\text{s}}$. It is a hot ($T = 9.29$ keV), massive ($\sim 2 \times 10^{15} M_{\odot}$), X-ray luminous ($L_X \sim 12.52 \times 10^{45} \text{ erg s}^{-1}$) cluster that is likely in a merger stage (Giovannini et al., 1999, Govoni et al., 2001).

Giovannini et al. (1999) first observed a 800 kpc regular shaped radio halo in A 773 with a ~ 14 mJy flux density at 1.4 GHz from the NRAO Very Large Array (VLA hereafter) Sky Survey (NVSS hereafter, Condon et al., 1998). The NVSS provides snapshot images of nearly all the sky north of Dec = -40° . However, its limited angular resolution ($45''$) and surface brightness sensitivity ($\sim 0.45 \text{ mJy beam}^{-1}$) made it difficult to separate the radio halo emission from the blend of point radio sources detected at the cluster centre.

Later, A 773 cluster was observed by Govoni et al. (2001) using VLA-C configuration at 1365 and 1435 MHz and VLA-D configuration at 1365 and 1665 MHz for a total of 2 hours in each configuration. This way, Govoni et al. (2001) obtained a better sensitivity and angular resolution with respect to the NVSS as well as a good sampling of short baselines - necessary to detect extended emission. The final VLA images of A 773 were created by adding together the two VLA-C configuration datasets together with the VLA-D configuration data at 1365 MHz. The VLA-D dataset obtained at 1665 MHz

was excluded from the imaging process due to corruption caused by interference. The high and low-resolution images had an angular resolution of $15''$ and $30''$ and noise levels of 0.02 and $0.03 \text{ mJy beam}^{-1}$ respectively.

Figure 1.9 shows the image of A 773 with a regular shaped, extended (1.5 Mpc) GRH with a flux density of 12.65 mJy at 1.4 GHz . The presence of a radio halo, coupled with the irregular and elongated shape of the X-ray emission (Figure 1.9) indicate that A 773 is in an active dynamic state. Deep (12 hour), follow up radio observations of A 773 cluster were conducted with the Westerbork Synthesis Radio Telescope (WSRT hereafter) at 18 cm and 21 cm . The aim of these observations is to:

1. Confirm the presence of a radio halo at the centre of A 773.
2. Study the radio halo physical properties (morphology, extent, flux density) at 18 cm and 21 cm .
3. Carry out a spectral index analysis of its radio halo.

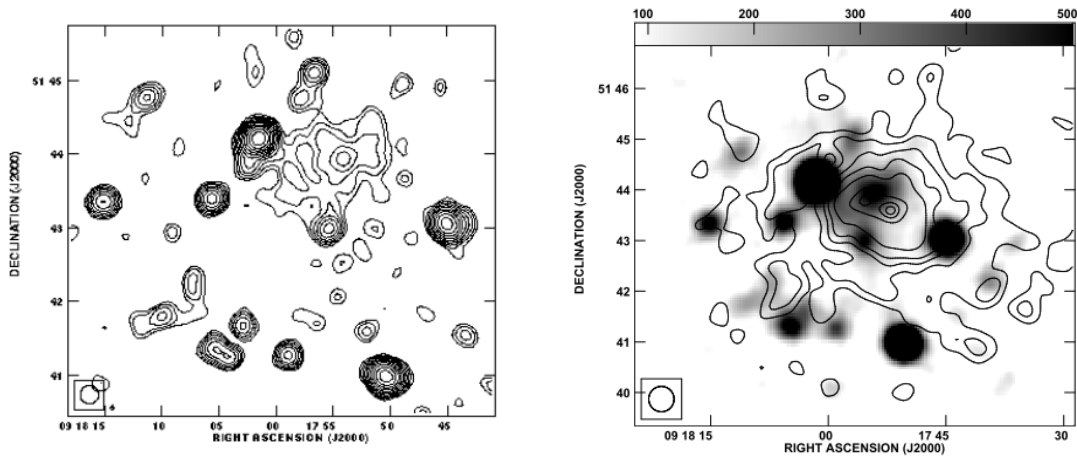


FIGURE 1.9: *Left panel:* 1.4 GHz radio image of the radio halo at centre of A773. The angular resolution is $15'' \times 15''$ and the noise level is $0.02 \text{ mJy beam}^{-1}$. Contour levels are: $-3, 3, 4, 6, 8.5, 12, 17, 24, 34, 48, 68, 96, 136, 192, 272, 384, 543 \times \sigma$. *Right panel:* X-ray contour plots of centre of A 773 cluster taken from the ROSAT archive overlapped to the 1.4 GHz greyscale image of centre of A 773 cluster with angular resolution of $30''$. The X-ray contours are: $0.65, 0.8, 1, 1.5, 3, 3.4, 3.6 \text{ Counts/pixel}$.

The thesis is organized in the following way. In chapter 2, we provide an overall introduction to radio interferometry. We give a concise description of how a two-element interferometer operates including interferometric calibration and imaging.

In chapters 3 and 4, we present Westerbork observations of A 773 galaxy cluster at 18 cm and 21 cm . After flagging and calibration, we proceeded to create high-resolution maps of the field for the purpose of identifying compact sources that were subtracted from the

data. Low resolution, high brightness sensitivity images were made to detect the radio halo.

In chapter 5 we present a combined analysis of the 18 cm and 21 cm observations of A 773. We then present our conclusions, including the limitations of the current work.

Chapter 2

Introduction to radio interferometry

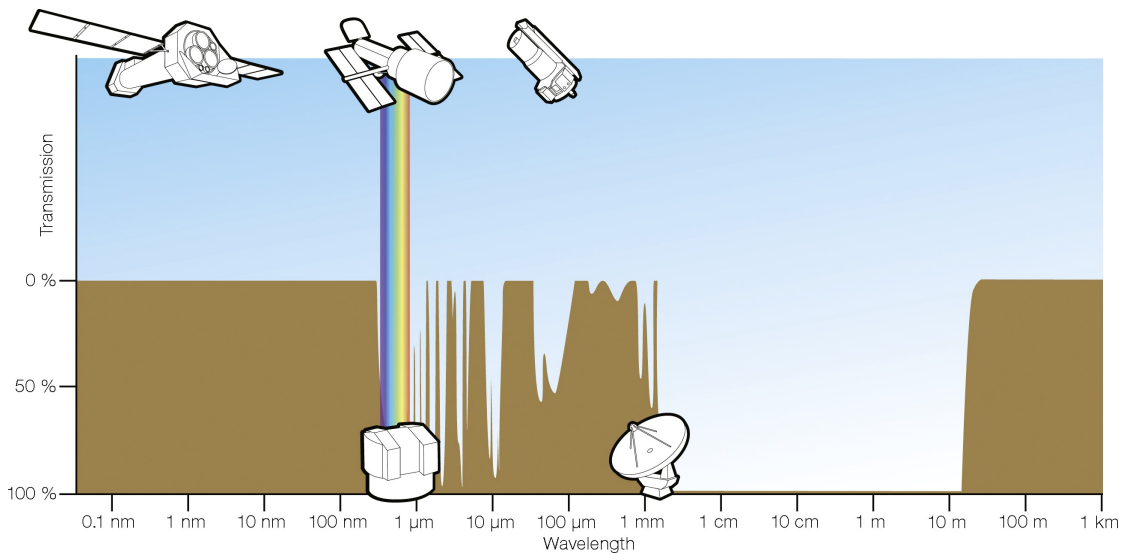


FIGURE 2.1: Schematic diagram of transmission of celestial electromagnetic radiation through Earth's atmosphere. The clear zone lying between $\lambda \sim 0.3$ mm and $\lambda \sim 30$ m depicts the so called 'radio window' through which celestial radio waves are observable from Earth (Condon & Ransom, 2016).

The Earth's atmosphere is opaque to a large range of electromagnetic wavelengths but mostly transparent in the radio regime (Figure 2.1). Radio telescopes were initially limited by their poor angular resolution θ , i.e. by the capability to separate two nearby sources:

$$\theta \approx \frac{\lambda}{D} \quad (2.1)$$

where λ is the observing wavelength and D is the diameter of the dish telescope. In the case of the $D = 305$ m Arecibo telescope - the largest radio telescope - , the angular resolution is only ~ 2.2 arcminutes at $\nu \approx 1.5$ GHz (or $\lambda \approx 20$ cm), worse than a

human eye ($\theta_{\text{eye}} \sim 50$ arcseconds). The development of the interferometric technique alleviates this problem by using an array of antennas distributed over large distances and combining the signals from antenna pairs. This process “synthesizes” a single dish of angular resolution:

$$\theta \approx \frac{\lambda}{B_{\text{max}}} \quad (2.2)$$

where B_{max} is the maximum separation between antenna pairs. In the following sections I will provide an overview of interferometry and the related image formation largely based on the [Thompson et al. \(2017\)](#) book.

2.1 The two-element interferometer

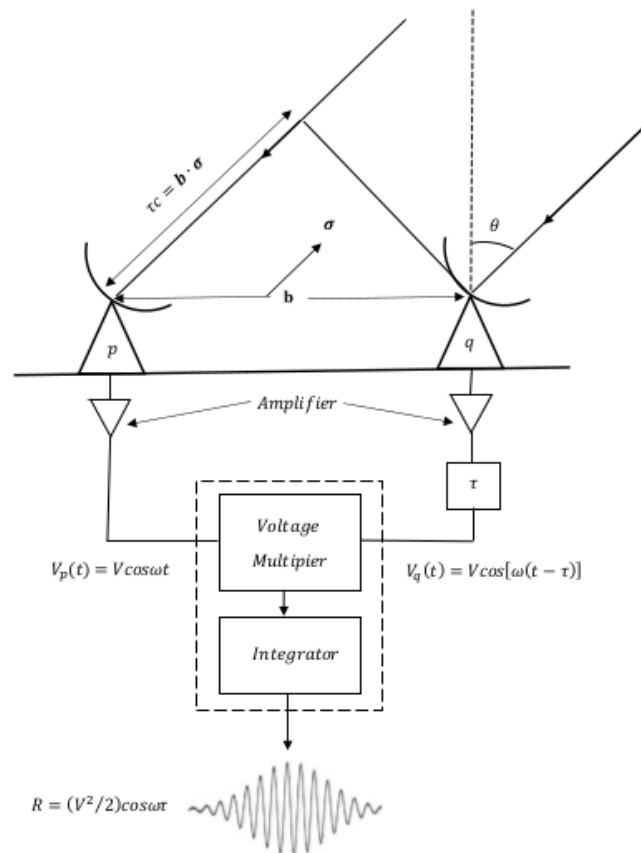


FIGURE 2.2: A schematic diagram of a two-element interferometer. Antennas are labeled p and q . The dashed-line box indicates the correlator, the digital equipment that performs the cross-multiplication and average of the antenna signals (from [Condon & Ransom, 2016](#)).

The simplest interferometer is the two-element interferometer (Figure 2.2). When both elements observe a sky source, the celestial radiation reaches the second element p with

a delay τ with respect to the first element q :

$$\tau = \frac{\vec{\mathbf{b}} \cdot \hat{\sigma}}{c} \quad (2.3)$$

where $\vec{\mathbf{b}}$ is the baseline vector between the two telescopes (i.e. the separation between them), $\hat{\sigma}$ is the unit vector in the direction of the source and c is the speed of light. This delay is often referred to as geometrical delay because it essentially depends upon the relative position of the antennas and the sky source. The phase associated to the geometrical delay can be expressed as:

$$\phi = \omega\tau = \frac{2\pi}{\lambda} \vec{\mathbf{b}} \cdot \hat{\sigma} \quad (2.4)$$

where λ is the observing wavelength. The celestial radiation induces voltages V_p and V_q that are proportional to the amplitude of the celestial signal E and can be written in a general form as:

$$V_p(t) = E \cos \omega t, \quad V_q(t) = E \cos[\omega(t - \tau)] \quad (2.5)$$

The voltages are then correlated:

$$\langle V_p V_q \rangle = \langle E^2 [\cos[\omega(t - \tau)] \cos \omega t] \rangle = E^2 \langle [\cos(\omega t) + \cos(2\omega t - \omega\tau)] \rangle \quad (2.6)$$

where brackets indicate a time average. The terms depending upon ωt oscillate much faster and typically average to zero leaving with:

$$\langle V_p V_q \rangle = \left(\frac{E^2}{2} \right) \cos(\omega\tau). \quad (2.7)$$

The correlator response varies sinusoidally as the Earth's rotation changes the source direction relative to the baseline vector $\vec{\mathbf{b}}$. These sinusoids are called fringes and the correlator can be thought of 'casting' a fringe pattern of $(2\pi \vec{\mathbf{b}}' \cdot \hat{\sigma})$ period onto the sky, where $\vec{\mathbf{b}}' = \frac{\vec{\mathbf{b}}}{\lambda}$.

Generally, the correlator can measure both the even (cosine) and odd (sine) fringes, leading to a complex fringe:

$$V' = \langle V_p V_q^* \rangle = \frac{E^2}{2} [\cos \omega\tau - \imath \sin \omega\tau] = \frac{E^2}{2} e^{-2\pi \imath \vec{\mathbf{b}}' \cdot \hat{\sigma}}. \quad (2.8)$$

If the above equation is integrated over the source size, it leads to the well known Van Cittert-Zernike theorem (Thompson et al., 2017):

$$V(\vec{\mathbf{b}}') = \iint_{\Omega} I(\hat{\sigma}) e^{-2\pi i \vec{\mathbf{b}}' \cdot \hat{\sigma}} d\hat{\sigma}, \quad (2.9)$$

where $I = \frac{E^2}{2}$, and Ω is the source area. If the baseline is expressed in terms of (u, v) coordinates and the source distribution in terms of direction cosines (l, m) , equation 2.9 can be re-written as a two dimensional Fourier transform:

$$V(u, v) = \iint_{\Omega} I(l, m) e^{-2\pi i (ul + vm)} dl dm. \quad (2.10)$$

Equation 2.10 is the cornerstone of interferometry and indicates that the measured visibilities, $V(u, v)$, are the Fourier transform of the sky brightness distribution. The sky brightness distribution can be recovered by inverting equation 2.10. A reliable reconstruction of the sky brightness distribution requires to sample the Fourier transform as densely as possible, i.e. sampling many (u, v) points. This is achieved by both constructing interferometers with many antennas that have many different separations as well as using the rotation of the Earth to continuously change the projected baselines between antenna pairs in the direction of the source, leading to an increase in (u, v) sampling in a process called Earth synthesis.

2.2 Introduction to calibration and imaging

Visibilities measured by any radio interferometric array are never an ideal measurement of the sky brightness distribution, but are corrupted by both the effects of the Earth's atmosphere and by the instrumental receiving chain. Other important reasons for data corruption are antenna malfunctioning and terrestrial interference in the form of radio frequency interference (RFI) from mobile devices and artificial satellites orbiting the Earth.

The process of editing out corruptions due to antenna malfunctioning and RFI from radio interferometric datasets is generally called *flagging*. Radio interferometric data from malfunctioning antennas, channels corrupted by RFI, zero amplitude data or any data taken at low elevations which is often unreliable and noisy are colloquially referred to as 'bad data' and need to be flagged from the data before proceeding with the science analysis.

The process of correcting for corruptions caused by propagation effects due to the Earth's atmosphere and by the instrumental receiving chain is called *calibration*. Signal corruptions are modelled using 2×2 complex matrices, called Jones matrices \mathbf{J} , that describe corruption for both polarization states of the incoming radiation. The corrupted visibilities can therefore be written as (Smirnov, 2011):

$$\mathbf{V}_{pq}(u, v) = \mathbf{J}_p \left(\iint_{\Omega} \mathbf{B} e^{-2\pi i(ul+vm)} dldm \right) \mathbf{J}_q^H, \quad (2.11)$$

where (p, q) indicate antennas, \mathbf{B} is the matrix that describes the polarization state of the celestial signal in terms of Stokes parameters (I, Q, U, V) :

$$\mathbf{B} = \begin{bmatrix} I + Q & U + iV \\ U - iV & I - Q \end{bmatrix}, \quad (2.12)$$

and H is the Hermitian operator. If the brightness matrix \mathbf{B} is known, as for example is the case of a calibration source, then calibration solves for the antenna based matrices \mathbf{J} . Jones matrices can generally be decomposed in time and frequency dependent matrices with each effect described by its own particular Jones matrix, for example like the matrix \mathbf{E} describing the telescope primary beam response. In the case where the original signal is first modulated by the primary beam before the antenna based complex gain is applied by the amplifier, the Jones chain is obtained by simply multiplying \mathbf{E} and \mathbf{G} Jones matrices together:

$$\mathbf{J} = \mathbf{G}\mathbf{E} \quad (2.13)$$

Calibration is often divided into first generation calibration (1GC), second generation calibration (2GC) and third generation calibration (3GC). 1GC is performed by observing a calibrator (i.e. sources with known parameters such as flux density, shape and spectrum) interspersed with observations of the target field. This allows us to use calibrator observations to track variations in the system response. Thus, calibrator observations can be used to calibrate for a variety of propagation effects to obtain calibration solutions which in turn, can be transferred to the target field.

The absolute flux density (i.e. the true flux of sources in the field) is calibrated by observing a *primary calibrator* (i.e. a strong point source with a known, constant flux density and spectrum) a few times during the observation run. Primary calibrators are relatively rare and are often far away from the target field. To calibrate the time variation of the instrument gains $\mathbf{G}(t)$, a *secondary calibrator* (i.e. a strong point-like source located sufficiently close to the target in the sky) is observed periodically for short durations.

After 1GC calibration, the target visibilities are Fourier transformed into a “dirty” image I_D , i.e. an image that still includes the telescope sampling function. In the interferometric case, the sampling function is the sampling of the (u, v) plane. The observed sky brightness distribution I_D is then given by:

$$I_D = PSF \circledast I_I \quad (2.14)$$

where PSF is the Point Spread Function (i.e. the Fourier transform of the interferometric sampling function), \circledast the convolution operation and I_I the intrinsic sky brightness distribution.

The intrinsic sky brightness distribution can be recovered through deconvolution from the PSF. The most used deconvolution algorithm in radio interferometry is called CLEAN (Högbom, 1974). The simplest CLEAN algorithm can be described as follows (Cornwell et al., 1999):

1. Initialize the model image to an empty copy of the “dirty” image and the residual image to a copy of the “dirty” image;
2. Identify the peak in the “dirty” image f_{\max} ;
3. Subtract a replicated PSF shifted at the peak location with intensity γf_{\max} , where $\gamma \sim 0.1 - 0.2$ is called loop gain;
4. Add a clean component of intensity γf_{\max} to the model image. Update the residual image;
5. Repeat from 2 but now on the residual image, unless the peak of the residual image is smaller than the user-specified threshold or the user-specified number of iterations was reached;
6. Construct a restored image by convolving the model image with a two dimensional Gaussian function fitted to the main lobe of the PSF and adding the residual image.

Clark (1980) developed a variant of the Högbom CLEAN known as Clark CLEAN, aimed at taking advantage of two dimensional Fast Fourier Transforms (FFT). Unlike the Högbom CLEAN, the Clark CLEAN iteration has a “major” cycle with a nested “minor” cycle. Inside the “minor” cycle, a modified Högbom CLEAN is used to find CLEAN components using only a small fraction of the PSF. This significantly increases computation speed in the “minor” cycle for large images. As the search is terminated, the “major” cycle begins and CLEAN components are fast Fourier transformed and correctly subtracted from the residual image.

Cotton and Schwab (Schwab, 1984) developed a variant of the Clark CLEAN (i.e., Cotton-Schwab CLEAN) where the CLEAN components are subtracted from the ungridded visibilities in the “major” cycle allowing for deconvolution across the entire image.

Images obtained with 1GC calibration are generally limited by variations of the instrumental response on time scales shorter than the cadence used to observe calibrators. Image quality is often defined in terms of dynamic range (i.e the ratio between the image peak flux f_{\max} and the noise σ_{rms}) can be improved even further by performing self-calibration (2GC) (Ekers, 1984, Pearson & Readhead, 1984). A 2GC calibration routine typically proceeds as follows:

1. an initial sky-model of the target field is created by deconvolving a 1GC calibrated image;
2. the sky-model is used to improve the time variations of the instrument gains;
3. a new, more complete sky model is derived from the deconvolution of self-calibrated visibilities;
4. calibration and deconvolution loops are iterated until convergence is achieved.

2.3 Westerbork Synthesis Radio Telescope

The Westerbork Synthesis Radio Telescope (WSRT) is a one-dimensional (1D) aperture synthesis telescope operated by the Netherlands Institute for Radio Astronomy (ASTRON). It consists of 14 steerable dish-shaped antennas of 25 m diameter on an East-West baseline. Ten WSRT antennas labelled from 0 to 9 are fixed 144-m apart and four antennas labelled A to D are on a movable rail track on the eastern end (Figure 2.3). Each antenna is on an equatorial mount.

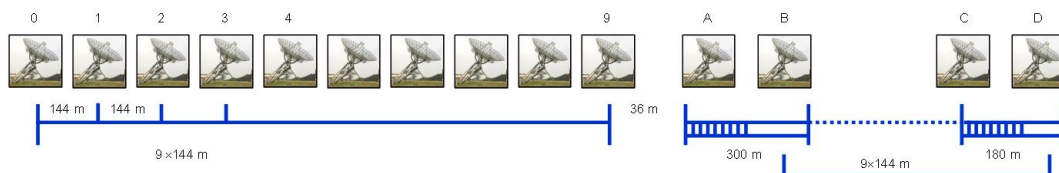


FIGURE 2.3: The layout of the 14 WSRT dishes.

The WSRT can observe in five different configurations, namely maxi-short, traditional, 2×48 , mini-short and 2×96 . In the maxi-short configuration, the antenna distance 9-A is 36 m, while A-B and C-D are 54 m and 72 m apart respectively. In traditional

configurations the A-9 distance can be moved incrementally by 12 m starting from 36 up to 96 m while distances A-B and C-D are fixed at 72 m. The combination of all these configurations cancels the grating lobes to the regular spacings across the whole field of view, at the cost of an increased observing time. The maxi-short configuration offers a good sensitivity to extended emission and a PSF with relatively low sidelobes in a reduced observing time.

Chapter 3

Observations of Abell 773 at 18 cm

3.1 Observations and data reduction at 18 cm

In this chapter, we present observations of A 773 taken with the WSRT at 18 cm (or 1713 MHz) on 31 January 2011 with the aim of studying the physical properties of the radio halo located at its centre.

The A 773 galaxy cluster was observed starting at sunset, for a total of 12 hours. The 12 hours synthesis is employed at the WSRT to improve the uv coverage through Earth rotation synthesis. Observations were taken in the maxi-short configuration that offers good imaging performance to extended emission.

Observations were performed at the central frequency of 1713 MHz with a 146 MHz bandwidth, divided in 8 slightly overlapping sub-bands, each 20 MHz wide. Table 3.1 provides a summary of observational details.

In WSRT observations, it is standard practice not to observe a secondary calibrator throughout the run as the telescope is known to be very stable. Instead, two primary calibrators were observed at the beginning and at the end of the observing run. The primary calibrator source 3C48 was observed at the beginning of the observation run for ~ 15 minutes, followed by the target A 773 which was continuously observed for 12 hours. At the end of the observation run, the primary calibrator 3C286 was observed for ~ 15 minutes. The data reduction was done in CASA version 5.1.1-5 ([McMullin et al., 2007](#)). Each sub-band was split into an individual dataset for each source before proceeding with flagging and calibration.

TABLE 3.1: Summary of the 18 cm observational setup

Coordinates of the field centre (J2000)	R.A. = 9 ^h 17 ^m 59 ^s , Dec. = +51 ^d 43 ^m 48 ^s
Central observing frequency ν (MHz)	1713
Frequency range (MHz)	1640 - 1786
Number of spectral sub-bands	8
Central frequency of each sub-band (MHz)	1650, 1668, 1686, 1704 1722, 1740, 1758, 1776
Width of each sub-band (MHz)	20
Number of channels in each sub-band	64
Channel width (kHz)	312.5
Integration time (sec)	30

After a visual inspection of the variation of visibility amplitudes of the primary calibrators against frequency, antenna 6 was found malfunctioning and permanently flagged, along with the sub-band edges. Further automatic RFI flagging was done using the `tfcrop` option in the `flagdata` task (Martins & Rau, 2016). `Tfcrop` is an automatic flagging algorithm that detects outliers on the 2D time-frequency domain. The algorithm iterates through the data in chunks of time. For each chunk, the user’s visibility data are organized as 2D time-frequency planes, one for each baseline. After that, for each baseline, an average visibility spectrum is calculated by averaging the visibility amplitudes in the time dimension. Next, a piece-wise polynomial fit to the visibility spectrum is calculated, together with standard deviation, σ . By default, all points deviating from the fit by more than 3σ are flagged. The above routine is repeated for each baseline in the frequency domain.

3C48 was used as a bandpass calibrator, assuming a 14.4 Jy flux density at 1.65 GHz and a $\alpha = -0.84$ ¹ spectral index (Perley & Butler, 2017). Antenna-based complex gains as a function of frequency were solved for using the CASA task `bandpass` for each sub-band. An example of amplitude calibration solutions is shown in Figure 3.1. The calibrated visibility amplitudes for 3C48 at 1.65 GHz shown in Figure 3.2 clearly match the assumed 14.4 Jy flux density of 3C48 at this frequency.

We tested the bandpass stability across the night by applying bandpass solutions to an observed second calibration source, 3C286, which was observed after the target field. The amplitude of its calibrated visibilities is consistent with the expected value of 13.9 Jy at 1.65 GHz (Figure 3.3), indicating negligible time variation of the bandpass throughout the night. The bandpass solutions derived for 3C48 were therefore applied to the target field. As there was no observation of a secondary calibrator during the observing run, time-dependent gains were only corrected for during 2GC self-calibration.

¹ $S_\nu \propto \nu^\alpha$, where S_ν is the flux density and ν the observing frequency

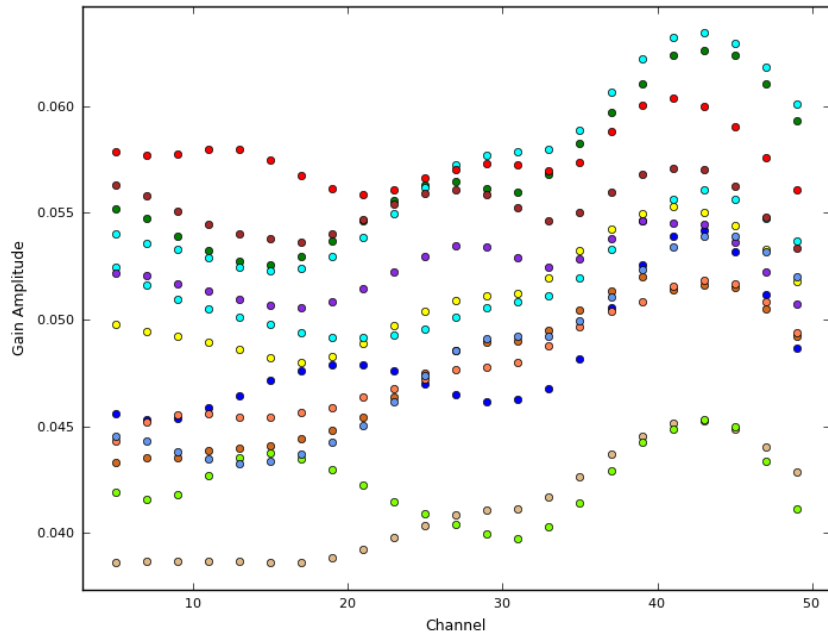


FIGURE 3.1: Example of bandpass solutions derived from 3C48 for the sub-band centred at 1.65 GHz. Each colour is a different antenna.

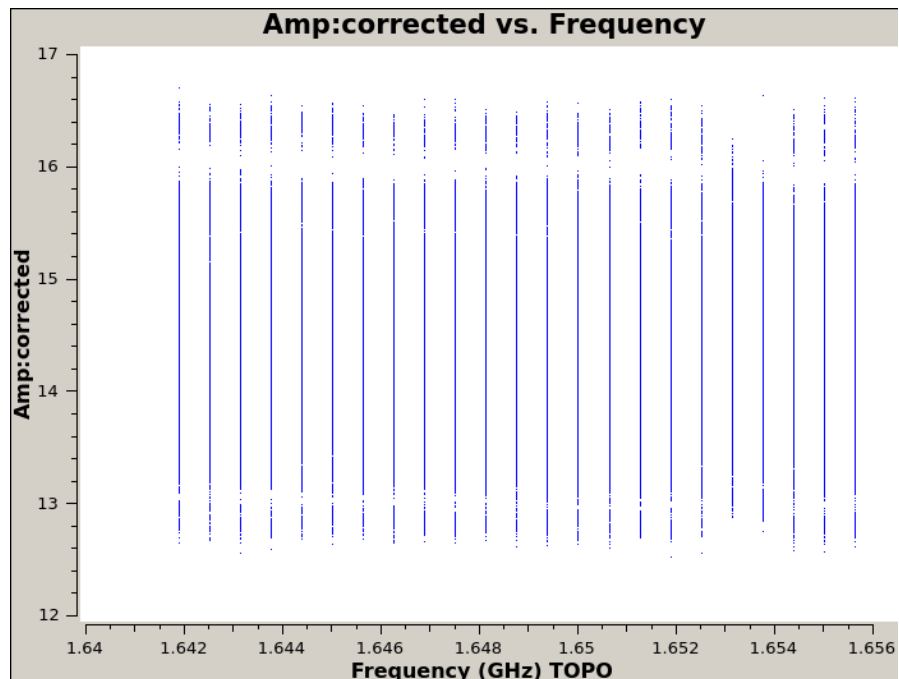


FIGURE 3.2: Calibrated visibility spectrum of 3C48 at 1.65 GHz. Their average amplitude is consistent with the model value (14.4 Jy).

The A 773 calibrated visibilities were Fourier transformed into a “dirty” image centred at central frequency of 1.713 GHz using the multi-frequency synthesis algorithm (Sault & Wieringa, 1994) and uniform weights in order to suppress sidelobes throughout the field of view. We imaged the whole field of view, corresponding to $1.4^\circ \times 1.4^\circ$ at 18 cm. The “dirty” image was then iteratively deconvolved using the Cotton-Schwab CLEAN

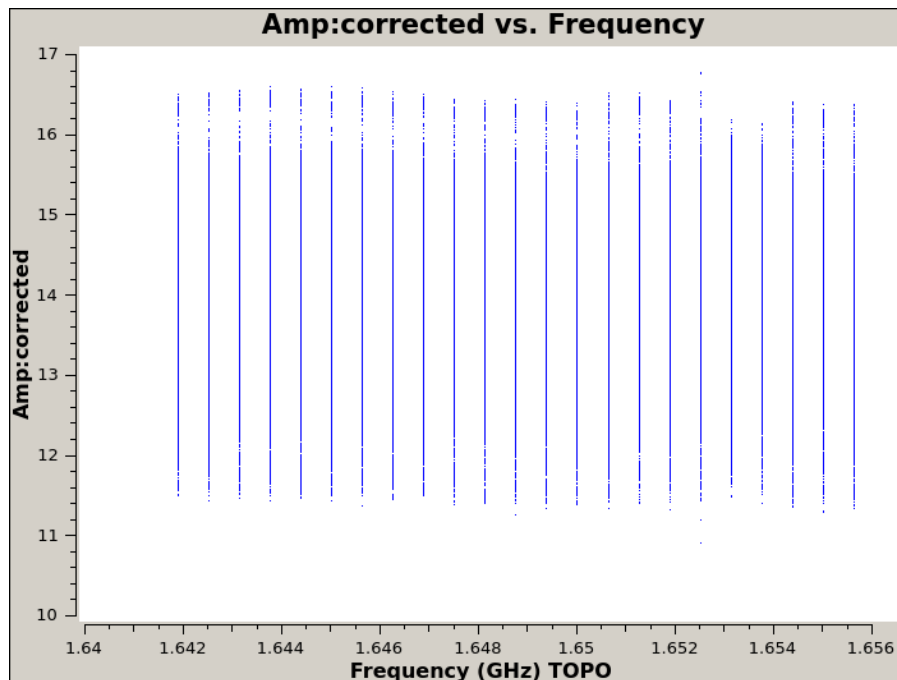


FIGURE 3.3: Calibrated visibility spectrum of 3C286 at 1.65 GHz. There is a good agreement with the model amplitude (13.9 Jy).

algorithm (Cornwell et al., 1999) until the first negative component was found at 0.7 mJy threshold. The derived sky model was used to self-calibrate time-dependent variation of the antenna phases with a 120 second solution interval. Examples of solutions are shown in Figure 3.4.

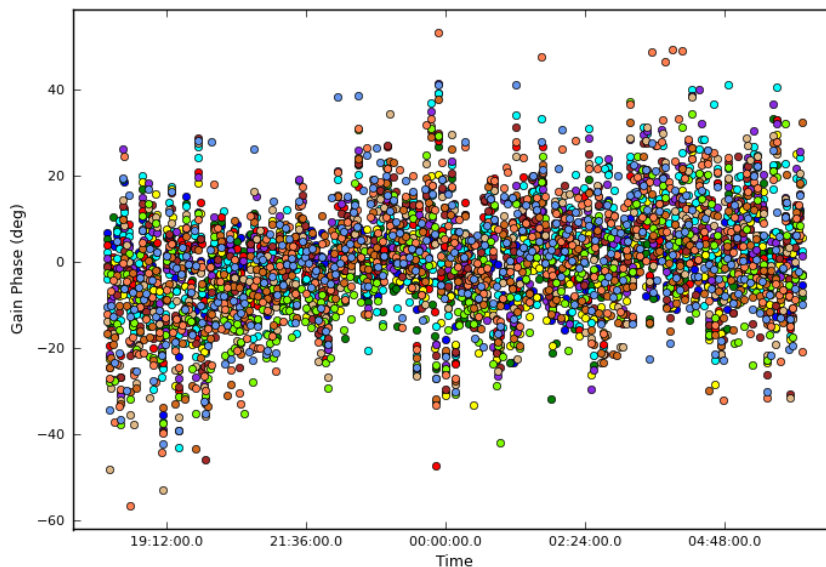


FIGURE 3.4: Self-calibration phase solutions. Each antenna is a different colour.

The self-calibrated visibilities of A 773 were imaged and deconvolved down to a flux density threshold of 0.4 mJy, where another negative component was found, after which a mask that included all the sources brighter than $200 \mu\text{Jy}$ was created to restrict the

deconvolution within these regions down to a $60 \mu\text{Jy}$ threshold. The final deconvolved image shown in Figure 3.5 has a noise level of $0.03 \text{ mJy beam}^{-1}$. The image essentially shows radio emission from compact-like sources with no evidence of diffuse emission at the centre (Figure 3.6).

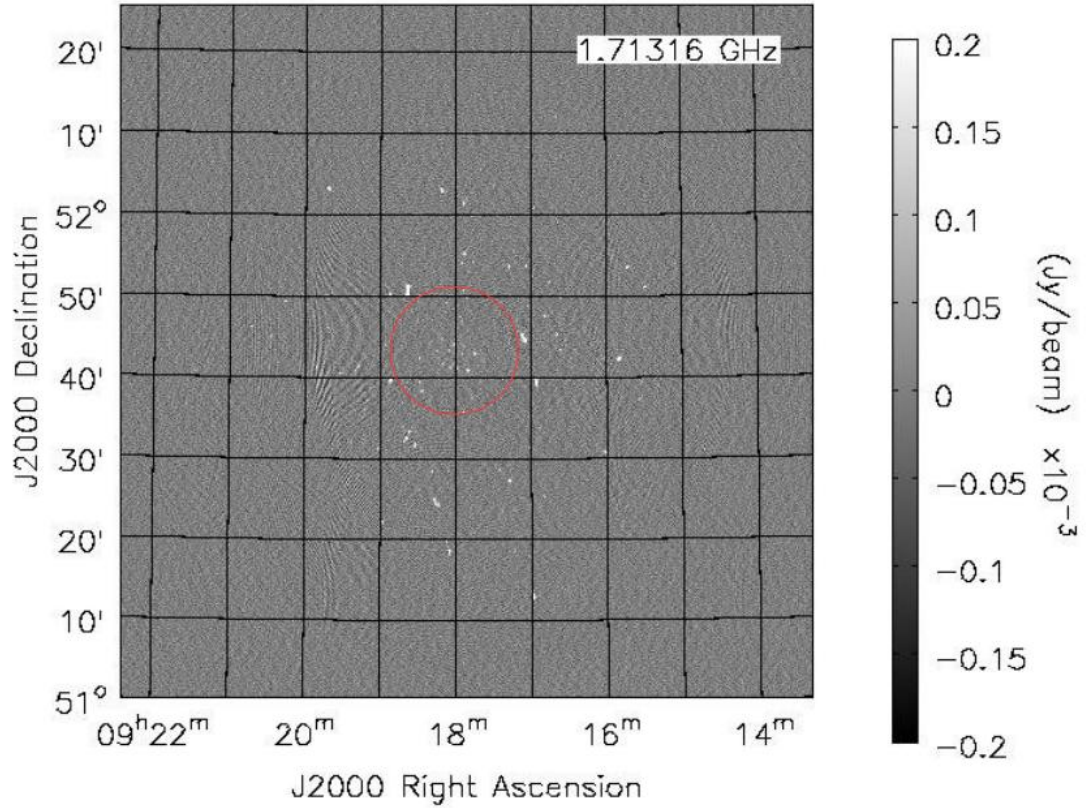


FIGURE 3.5: Uniform weighted image of the A 773 field at 18 cm. The image is not primary beam corrected. The angular resolution is $11'' \times 9''$ and the noise level $0.03 \text{ mJy beam}^{-1}$. The red circle in the centre indicates the cluster Abell radius ($\sim 8'$).

In order to highlight the potential presence of diffuse emission at the cluster centre, we proceeded with the identification and successful subtraction of all the compact sources down to $60 \mu\text{Jy}$ in order to image the residual visibilities at lower resolution and improve the brightness sensitivity. The sky model was Fourier transformed and subtracted from the self-calibrated visibilities in order to form a set of residual visibilities that were imaged using different weighting schemes (Briggs, 1995). We generated residual images with robust parameter $r = 0, 0.5$ and 0.75 respectively (Figure 3.7). The variations of radio properties of the radio halo at centre of A 773 as a function of r are listed in Table 3.2. Diffuse emission becomes more visible at the cluster centre with increasing value of r . Although there is no hint of diffuse emission in the $r = 0$ map, a small, extended source (0.87 arcmin^2 , corresponding to 12 synthesized beams) is visible in the $r = 0.5$ map (middle panel of Figure 3.7).

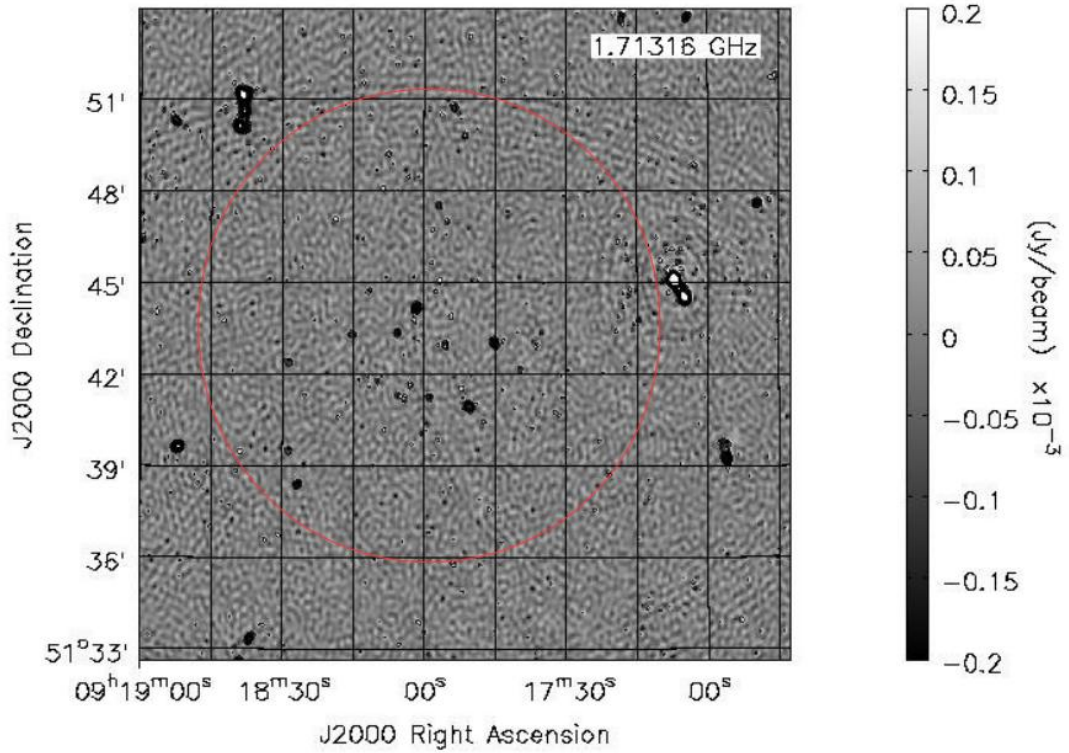


FIGURE 3.6: Zoom into the centre of Figure 3.5. Contours (black) showing the compact radio sources are drawn at $-3, 3, 6, 9, 12, 15, 18, 24, 30, 36, 42, 48, 54, 60, 66 \times \sigma$. The red circle denotes the cluster Abell radius ($\sim 8'$).

TABLE 3.2: Radio properties of radio halo at centre of A 773 cluster as a function of r at 18 cm.

r	synthesized beam size	image noise mJy beam^{-1}	halo area arcmin^2	linear size arcmin	number of beams	S_ν mJy
-2	$11'' \times 9''$	0.03	—	—	—	—
0	$14'' \times 11''$	0.02	—	—	—	—
0.5	$18'' \times 14''$	0.02	0.87	1.70	12	$1.42 \pm 2\%$
0.75	$19'' \times 15''$	0.02	5.88	3.68	74	$8.82 \pm 3\%$

Diffuse emission is clearly evident in the $r = 0.75$ map, with contour levels up to ten times the noise (Figure 3.7 *Bottom panel*). It extends over ~ 3.68 arcmin (1 Mpc linear size), with an area corresponding to 5.88 arcmin^2 (~ 74 synthesized beams) and a $8.82 \pm 3\%$ mJy integrated flux density at 1.713 GHz. We also imaged the residual visibilities using natural weights, which give the best brightness sensitivity. We noted, however, that for robust parameters $r \geq 1$, images start to suffer from substantial contribution of grating lobes, due to the regular configuration of the array. Grating lobes make it difficult to estimate the noise level of the image and make the estimates obtained at the edge of the field, where the sky emission is suppressed by the primary

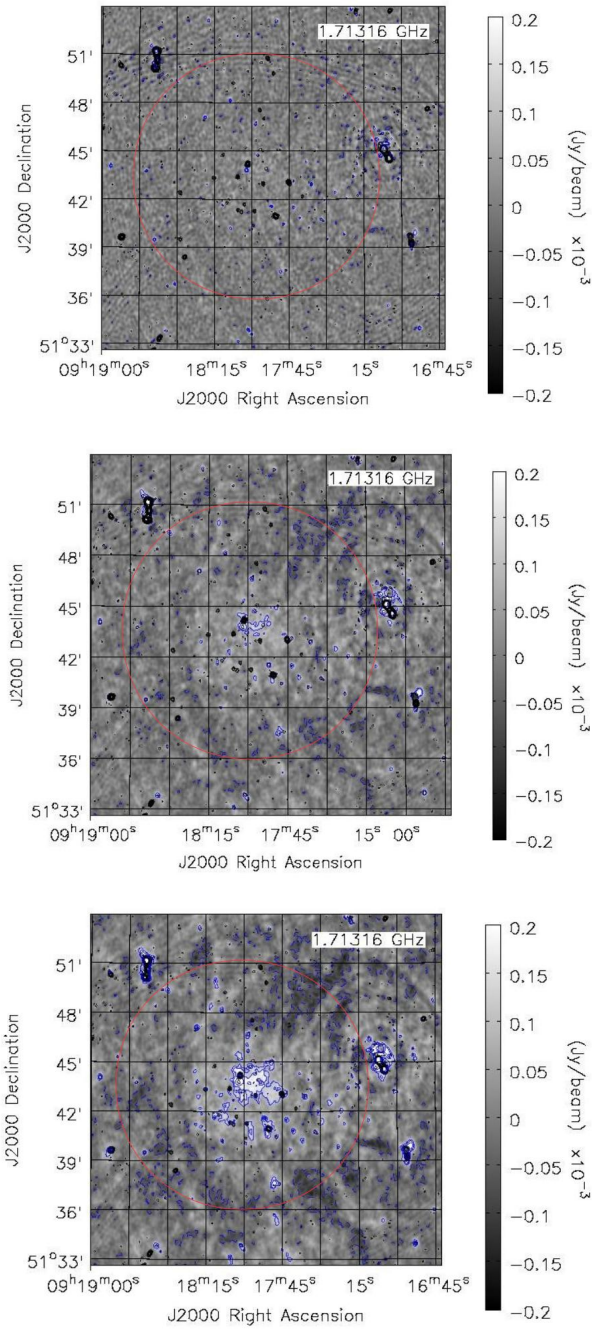


FIGURE 3.7: Low resolution, 1.713 GHz radio images of A 773 with robust parameter $r = 0, 0.5, 0.75$ (see text for details) after subtraction of point sources (black contours). In all images, the noise level is $0.02 \text{ mJy beam}^{-1}$ and contours (blue) are drawn at $-3, 5$ and $7 \times \sigma$ respectively. *Top panel:* $r = 0$ image, the angular resolution is $14'' \times 11''$. *Middle panel:* $r = 0.5$ image, the angular resolution is $18'' \times 14''$. *Bottom panel:* $r = 0.75$ image, the angular resolution is $19'' \times 15''$.

TABLE 3.3: Radio properties of radio halo at centre of A 773 as a function of uvrange at $r = 0.75$.

uvrange m	synthesized beam size	image noise mJy beam ⁻¹	halo area arcmins ²	linear size arcmins	number of beams	S_ν mJy
100	19'' × 15''	0.018	–	–	–	–
80	19'' × 15''	0.018	0.18	0.78	2	0.20 ± 15%
50	19'' × 15''	0.018	2.65	2.23	33	3.62 ± 0.8%

beam, unreliable at the image centre. We therefore consider the image obtained with the robust parameter $r = 0.75$ as the image with the best brightness sensitivity.

Low resolution images inevitably become sensitive to emission on scales much larger than the synthesized beam as well as confusion noise. Figure 3.7 (*Bottom panel*) indeed displays residual emission at the location of sources that appear accurately subtracted in the $r = 0$ image (Figure 3.7 *Top panel*), as well as sidelobe emission from these sources and general positive and negative fluctuations on scales of several arcminutes. Although part of this pattern seems to be due to sidelobes, it cannot be excluded that part is genuinely due, for example, to Galactic diffuse emission that may have power on such scales (e.g., Bernardi et al., 2009). In particular, the radio halo appears to be seated on top of a “pedestal” of low surface brightness emission whose extent complicates the assessment about its significance.

We attempted to filter out some of the large scale emission by excluding the shortest baselines from the images. In particular, we imaged the residual visibilities using a robust parameter $r = 0.75$ and excluding baselines shorter than 100, 80 and 50 m respectively. As is evident from Table 3.3, there is no diffuse radio emission present at the cluster centre when only baselines greater than 100 m were included. This means that the diffuse radio emission visible in Figure 3.7 (*Bottom panel*) is associated with baselines shorter than 100 m, which correspond to ~ 1.7 Mpc scales at $z = 0.217$. When baselines longer than 80 m are included, only marginal diffuse emission is detected. A clear detection is only obtained when baselines longer than 50 m are included.

As it can be seen in Figure 3.8, the shape of the diffuse radio emission at the cluster centre with the baseline cut at 50 m is more regular but significantly less extended compared to the image with no baseline cut. Conservatively, we adopted Figure 3.8 (*Bottom panel*) and the corresponding radio parameters in Table 3.3 as our most accurate assessment of the radio halo at the centre.

The radio halo appears regularly shaped with a linear extent of 2.23 arcmin (0.6 Mpc) corresponding to an area of 2.65 arcmin² with a 3.62 ± 0.8 mJy flux density at 1.713 GHz.

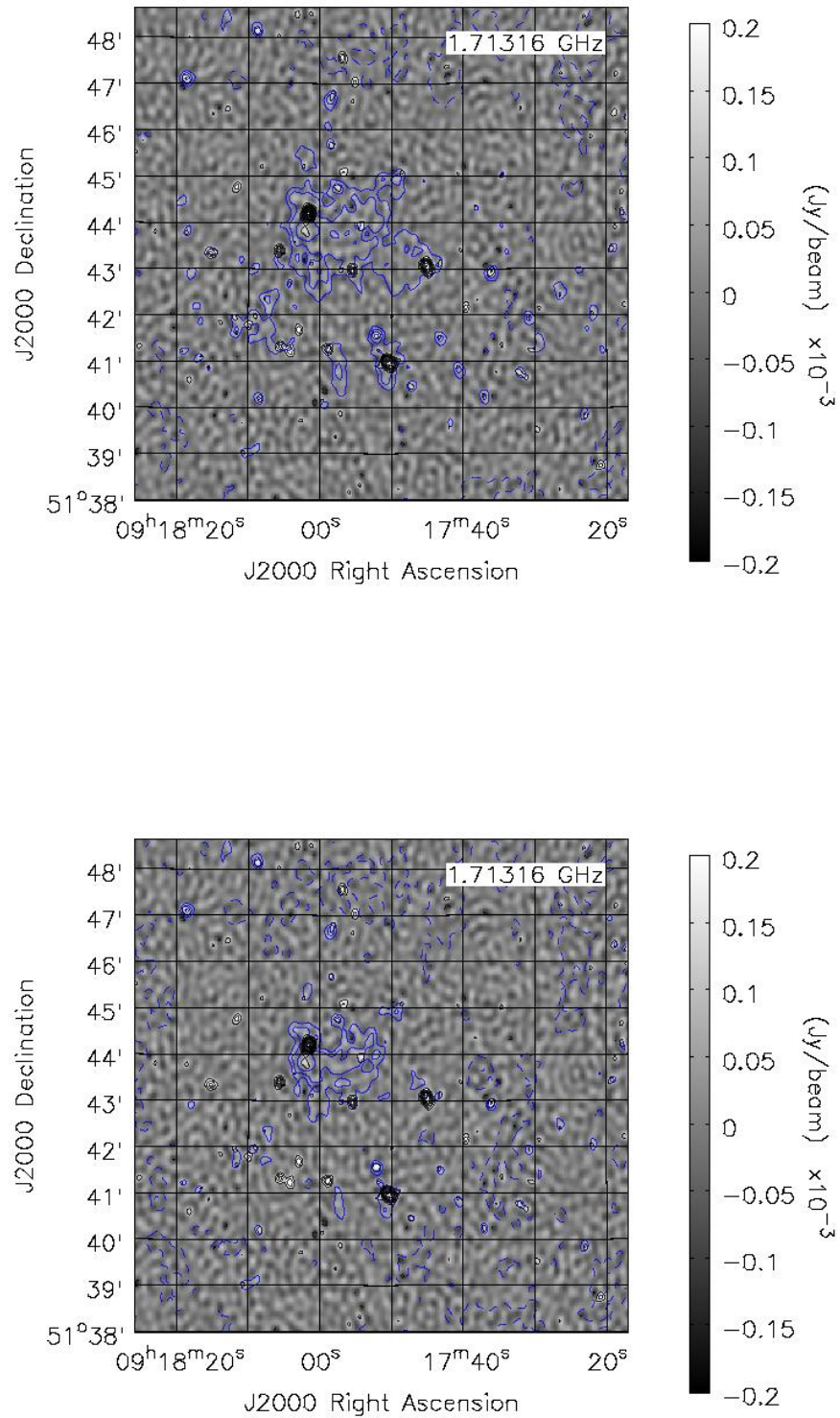


FIGURE 3.8: *Top panel:* Contours from the $r = 0.75$ image (Figure 3.7 *Bottom panel*) overlaid on the uniform weighted image (Figure 3.6). Contours are drawn at $-3, 5, 7$ and $10 \times \sigma$. *Bottom panel:* Contours from the $r = 0.75$ image with baselines longer than 50 m overlaid on the uniform weighted image (Figure 3.6). Contours are drawn at $-3, 5, 7$ and $10 \times \sigma$.

By visually comparing the shape and area of our radio halo to that detected by [Govoni et al. \(2001\)](#) shown in Figure 1.9 (*Left panel*), at 1.4 GHz with angular resolution of $15''$ and a noise level of $0.02 \text{ mJy beam}^{-1}$, a relatively good match in terms of morphology is found, although the extent in our images is $\sim 40\%$ than in [Govoni et al. \(2001\)](#) and the flux density is only $\sim 30\%$.

Chapter 4

Observations of Abell 773 at 21 cm

4.1 Observation and data reduction at 21 cm

In this chapter, we present observations of A 773 taken with the WSRT at 21 cm on 26 January 2011. Observations were carried out at the central frequency of 1380 MHz with a 146 MHz bandwidth, divided into eight slightly overlapping sub-bands, each 20 MHz wide. Table 4.1 includes a summary of the observational details. The calibration source 3C48 was observed at the beginning of the observation for 15 minutes. Thereafter, A 773 has observed for 12-hours in order to fill the *uv*-plane. As for the 18 cm observation, a secondary calibrator was not observed throughout the night since. At the end of the observation run, the primary calibrator 3C286 was observed for 15 minutes.

The data reduction was done in CASA version 5.1.1-5 (McMullin et al., 2007). Each sub-band was split into an individual dataset for each source before proceeding with flagging and calibration. Antenna 6 was flagged again along with the band edges. Further automatic RFI flagging was done using the `tfcrop` option in the `flagdata` task (Martins & Rau, 2016). About 30% of the data were flagged in total.

3C48 was used as a bandpass calibrator assuming a 16.5 Jy flux density at 1.41 GHz and a $\alpha = -0.84$ spectral index (Perley & Butler, 2017). Antenna-based complex gains as a function of frequency were solved for using the CASA task `bandpass`. An example of amplitude calibration solutions in Figure 4.1. Calibrated visibility amplitudes for 3C48 at 1.41 GHz shown in Figure 4.2 match the flux density predictions. We tested here again the bandpass stability across the night by applying bandpass solutions to the calibration source 3C286, which was observed after the target field. The amplitude of its calibrated

TABLE 4.1: Summary of the 21 cm observational setup

Coordinates of the field centre (J2000)	R.A. = $9^{\text{h}}17^{\text{m}}59^{\text{s}}$, Dec. = $+51^{\text{d}}43^{\text{m}}48^{\text{s}}$
Central observing frequency ν (MHz)	1380
Frequency range (MHz)	1301 - 1450
Number of spectral sub-bands	8
Central frequency of each sub-band (MHz)	1311, 1330, 1350, 1370 1392, 1410, 1432, 1450
Width of each sub-band (MHz)	20
Number of channels in each sub-band	64
Channel width (kHz)	312.5
Integration time (sec)	30

visibilities is consistent with the expected value of 15.2 Jy at 1.41 GHz, confirming the bandpass stability throughout the observation (Figure 4.3). The bandpass solutions were then used to calibrate the target field A 773.

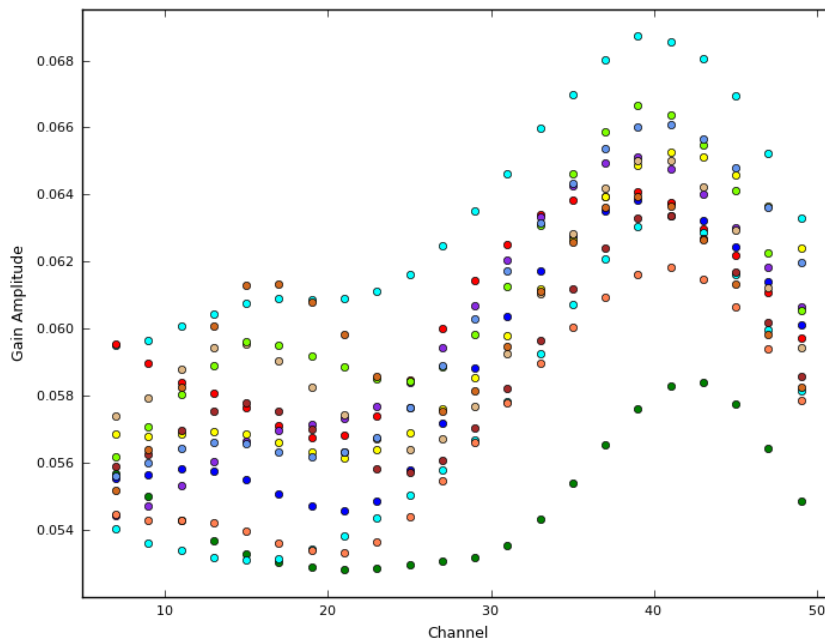


FIGURE 4.1: Example of bandpass solutions derived from 3C48 for the sub-band centred at 1.41 GHz. Each colour is a different antenna.

The calibrated visibilities were Fourier transformed into a “dirty” image centred at 1.38 GHz using the multi-frequency synthesis algorithm (Sault & Wieringa, 1994) and uniform weights in order to suppress sidelobes throughout the field of view. We imaged the whole field of view, corresponding to $1.4^{\circ} \times 1.4^{\circ}$ at 21 cm. The “dirty” image was then deconvolved using the Cotton-Schwab CLEAN algorithm (Cornwell et al., 1999) until the first negative component was found at the 1.2 mJy threshold. The derived sky

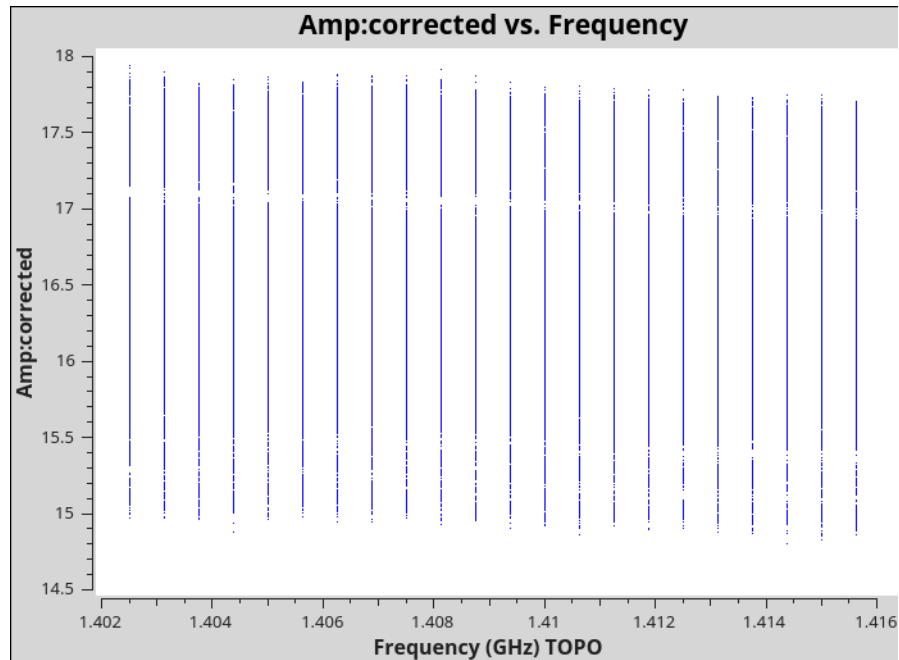


FIGURE 4.2: Calibrated visibility amplitude of 3C48 at 1.41 GHz. The average value of visibility amplitude is consistent with the model value of 16.5 Jy.

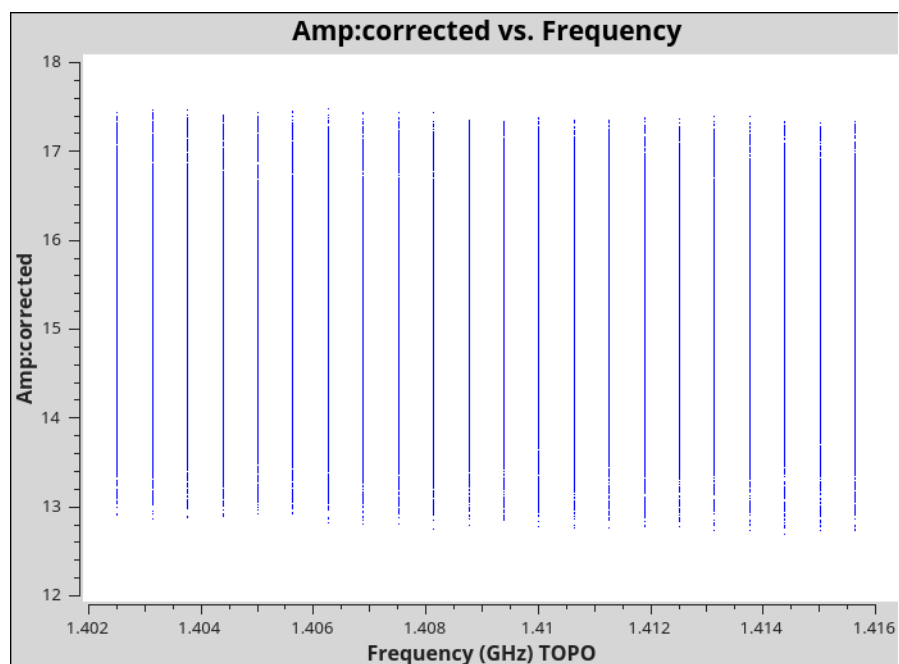


FIGURE 4.3: Calibrated visibility amplitude of 3C286 at 1.41 GHz. The average value of visibility amplitude matches the model flux density of 15.2 Jy.

model was used to self-calibrate time-dependent variations of the antenna phases with a 120 second solution interval. Examples of solutions are shown in Figure 4.4.

The self-calibrated visibilities were imaged and deconvolved down to a flux threshold of 0.4 mJy, where a negative component is added to the sky model, after which a mask that included all the sources brighter than 200 μ Jy was created to restrict the

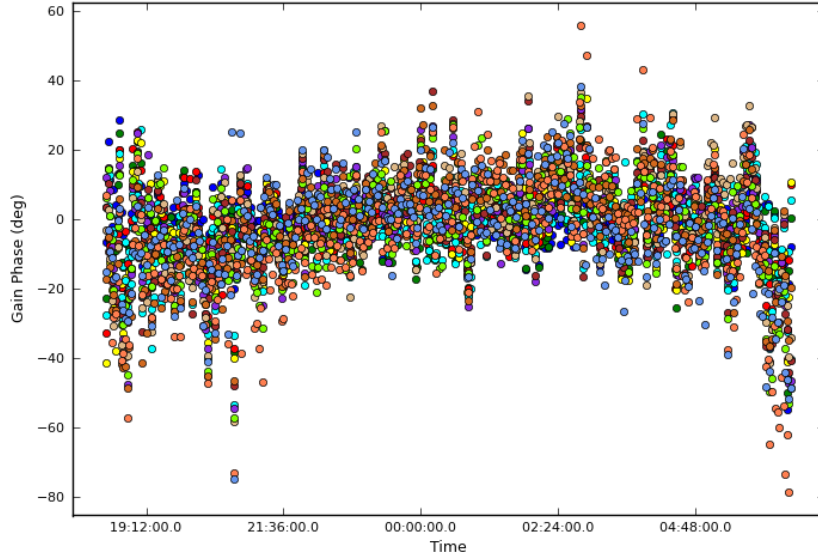


FIGURE 4.4: Phase behaviour of the self-calibration solutions at 1.41 GHz. Each antenna is a different colour.

deconvolution within these regions down to a $60 \mu\text{Jy}$ (2σ) threshold same as in the 18 cm data reduction. The final deconvolved image is shown in Figure 4.5. The image shows emission from compact-like sources with no evidence of diffuse emission at the cluster centre (Figure 4.6). The image also suffers from significant contamination by secondary sidelobes that appear to originate from the bright off-axis source visible at the bottom of the field of view. These ring-like secondary sidelobes in the 21 cm image are direction dependent effects likely caused by telescope pointing errors.

In order to highlight the potential presence of diffuse emission associated within the cluster centre, we followed the same procedure applied to the 18 cm data, i.e. we identified and subtracted compact sources and imaged the residual visibilities at lower resolution to improve the surface brightness sensitivity. In order to build a sky model of the compact radio sources in the field of view, the self-calibrated visibilities were first Fourier transformed into a “dirty” image and then deconvolved using the Cotton-Schwab CLEAN algorithm down to a $60 \mu\text{Jy}$ (2σ) threshold, where σ is the measured final image rms noise of $0.03 \text{ mJy beam}^{-1}$ measured in a small region far away from the centre of the final deconvolved image (Figure 4.5).

The sky model was Fourier transformed and subtracted from the self-calibrated visibilities in order to form a set of residual visibilities that were imaged using different weighting schemes (Briggs, 1995). We generated residual images with robust parameter $r = 0, 0.5$ and 0.75 (Figure 4.7), respectively. The variations of radio properties of the radio halo at centre of A 773 as a function of r are listed in Table 4.2. Like at 18 cm, we note that evidence of diffuse emission at the cluster centre increases with increasing

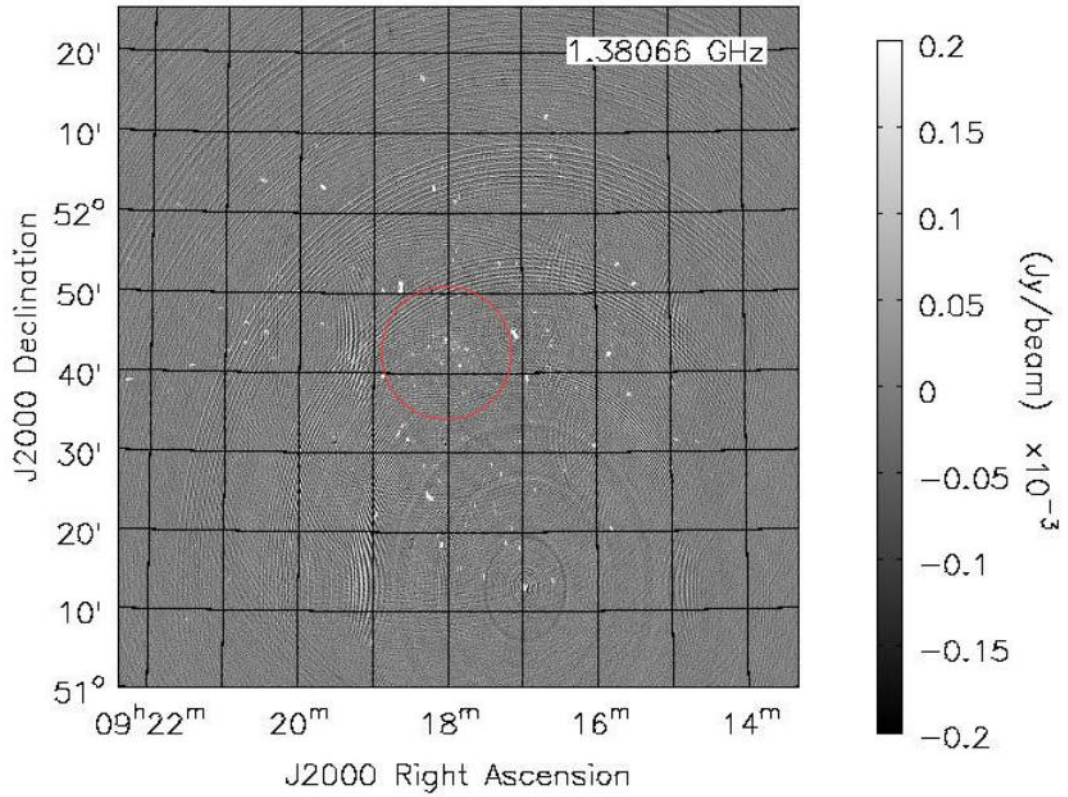


FIGURE 4.5: Uniform weighted image of the A 773 field at 21 cm. The angular resolution is $14'' \times 11''$ and the noise level is $0.03 \text{ mJy beam}^{-1}$. The red circle in the centre of the field indicates the cluster Abell radius $\sim 8'$.

TABLE 4.2: Radio properties of radio halo at centre of A 773 cluster as a function of r at 21 cm.

r	synthesized beam size	image noise mJy beam^{-1}	halo area arcmin^2	linear size arcmin	number of beams	S_ν mJy
-2	$14'' \times 11''$	0.030	–	–	–	–
0	$17'' \times 13''$	0.026	–	–	–	–
0.5	$21'' \times 16''$	0.026	1.92	2.4	20	$3.25 \pm 1\%$
0.75	$23'' \times 18''$	0.032	5.62	4.0	48	$10.1 \pm 0.5\%$

value of r , as expected. There is no hint of diffuse emission found in the $r = 0$ image (Figure 4.7 top panel). However, some extended diffuse radio emission (1.9 arcmin^2 , corresponding to 20 synthesized beams) is visible in the $r = 0.5$, with a flux density of 3.25 mJy (Figure 4.7 Middle panel).

Diffuse emission is clearly evident in the $r = 0.75$ map, with contour levels up to ten times the noise level (Figure 4.7 Bottom panel). The diffuse emission extends with a 4 arcmin linear size (or $\sim 1.1 \text{ Mpc}$ at $z = 0.217$), corresponding to a 5.6 arcmin^2 area (~ 48 synthesized beams) and an integrated flux density of 10.1 mJy . Also here,

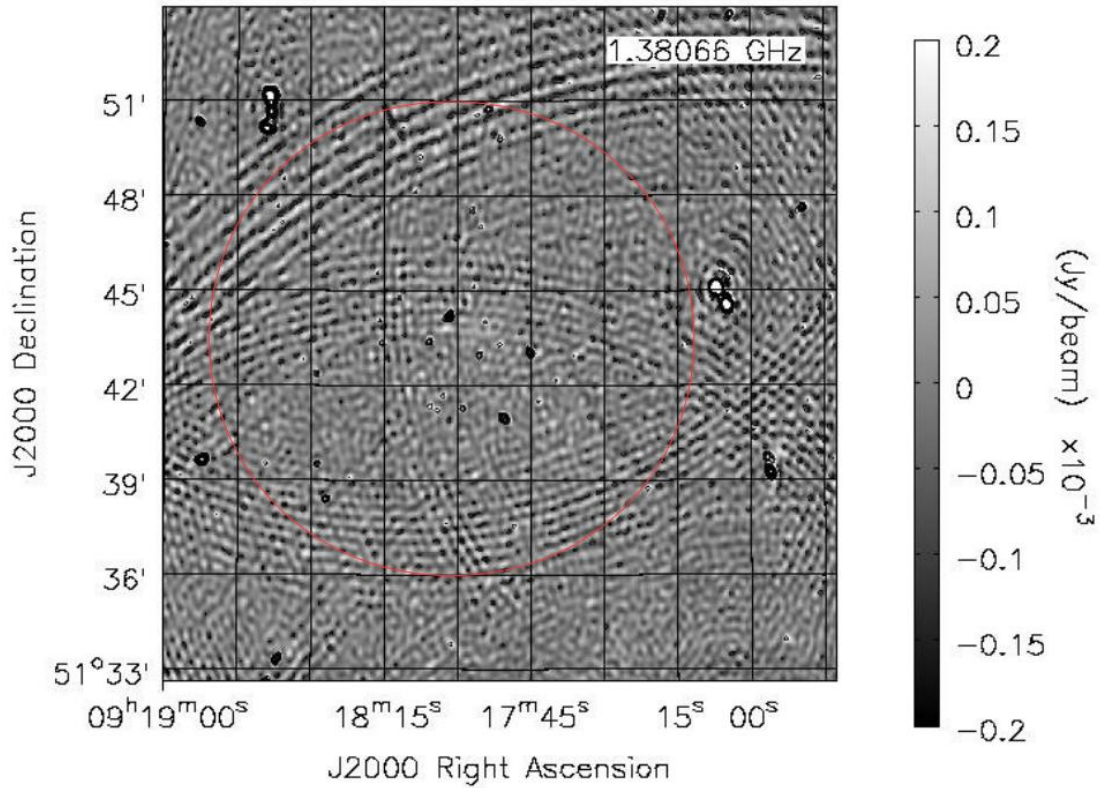


FIGURE 4.6: Zoom into the centre of Figure 4.5. Black contours showing the compact radio sources are drawn at $-3, 6, 9, 12, 15, 18, 24, 30, 36, 42, 48, 54, 60, 66 \times \sigma$. The red circle denotes the cluster Abell radius $\sim 8'$.

images made with robust parameters $r \geq 1$ suffer from contributions from grating lobes, therefore, as it was done for the 18 cm data, we thus considered the $r = 0.75$ radio image (Figure 4.7 *Bottom panel*) to be the image with the best brightness sensitivity. Our $r = 0.75$ radio image has an angular resolution of $20''$ and an rms noise level of $0.03 \text{ mJy beam}^{-1}$ which are similar to Govoni et al. (2001) ($15''$ and $0.02 \text{ mJy beam}^{-1}$ respectively).

The radio halo at the centre of Figure 4.7 (*Bottom panel*) has morphological similarities with the radio halo observed by Govoni et al. (2001) as shown in the left panel of their Figure 5 at the same frequency (see Figure 1.9 *Left panel*). The radio halo in our $r = 0.75$ images appears to have a regular shape and fairly extended just like in Govoni et al. (2001). The centre of the radio halo is clearly contaminated by rings of secondary sidelobes originating from the bright off-axis source south of the image centre.

As for the 18 cm images, our 21 cm images show positive and negative fluctuations on scales of several arcminutes. Also in these observations, we attempted to filter out some of the large scale emission by excluding the shortest baselines from the images. We imaged the residual visibilities using a robust parameter $r = 0.75$ and excluding baselines

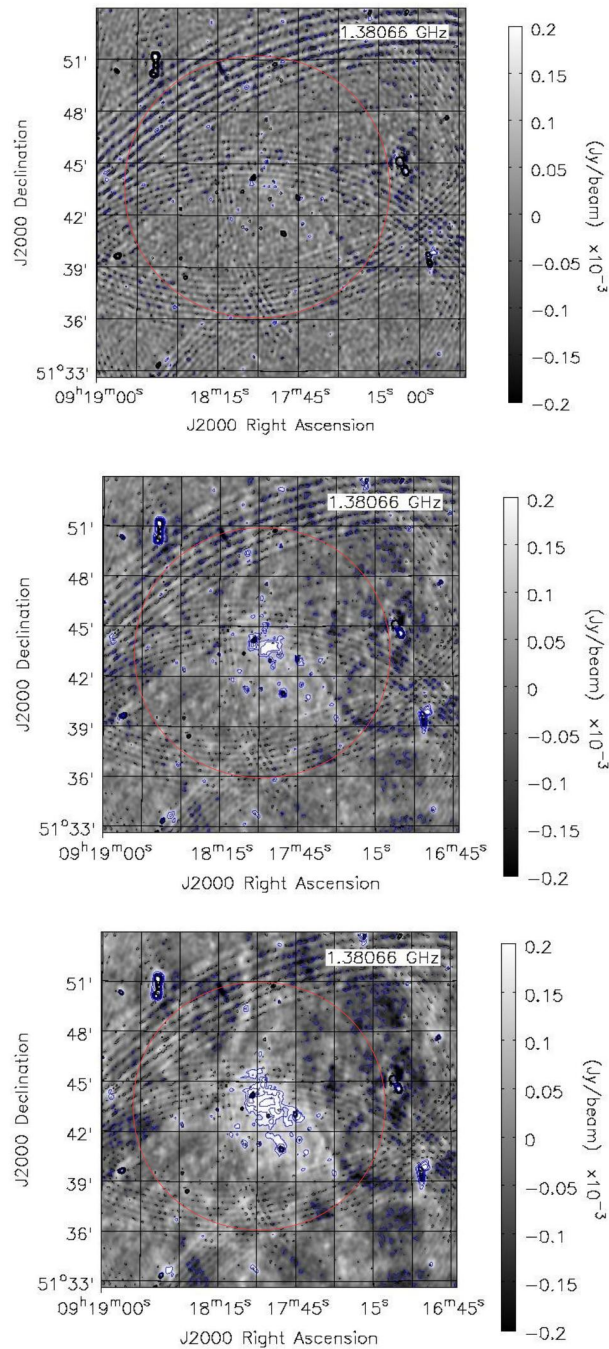


FIGURE 4.7: Low resolution, 1.38 GHz images of the A 773 cluster with different robust parameter values. *Top panel:* $r = 0$ image with $17'' \times 13''$ angular resolution and $0.026 \text{ mJy beam}^{-1}$ noise rms. Contours (blue) are drawn at $-3, 5$ and $7 \times \sigma$ respectively. *Middle panel:* $r = 0.5$ image, with a $21'' \times 16''$ angular resolution and $0.026 \text{ mJy beam}^{-1}$ noise rms. Contours (blue) are drawn at $-3, 5, 7$ and $10 \times \sigma$ respectively. *Bottom panel:* $r = 0.75$ image, with a $23'' \times 18''$ angular resolution and a $0.032 \text{ mJy beam}^{-1}$ noise rms. Contours are drawn at $-3, 5, 7$ and $10 \times \sigma$ respectively.

TABLE 4.3: Radio properties of radio halo at centre of A 773 as a function of uvrange at $r = 0.75$ at 21 cm.

uvrange m	resolution	image noise mJy beam^{-1}	halo area arcmins^2	linear size arcmins	number of beams	S_ν mJy
100	$22'' \times 13''$	0.026	1.10	2.1	14	$1.51 \pm 2\%$
80	$22'' \times 16''$	0.023	1.58	2.3	15	$2.24 \pm 2\%$
50	$23'' \times 18''$	0.025	3.76	2.9	34	$5.66 \pm 1\%$

shorter than 100, 80 and 50 m respectively. As is evident from Table 4.3, there is a marginal amount of diffuse radio emission present at the cluster centre when only baselines greater than 100 m were included. A clear radio halo detection is only obtained when baselines larger than 50 m are included, similar to the 18 cm case (Figure 4.8 *Bottom panel*).

As it can be seen in Figure 4.8, the shape of the diffuse radio emission at the cluster centre with the baseline cut at 50 m is more regular but significantly less extended compared to the image with no baseline cut. Conservatively we adopted the Figure 4.8 *Bottom panel* and the corresponding parameters in Table 4.3 as our most accurate assessment of the radio halo at the cluster centre at this frequency. It is ~ 0.8 Mpc wide, with a 5.66 mJy flux density, about two times fainter than what is reported by Govoni et al. (2001) at the same frequency.

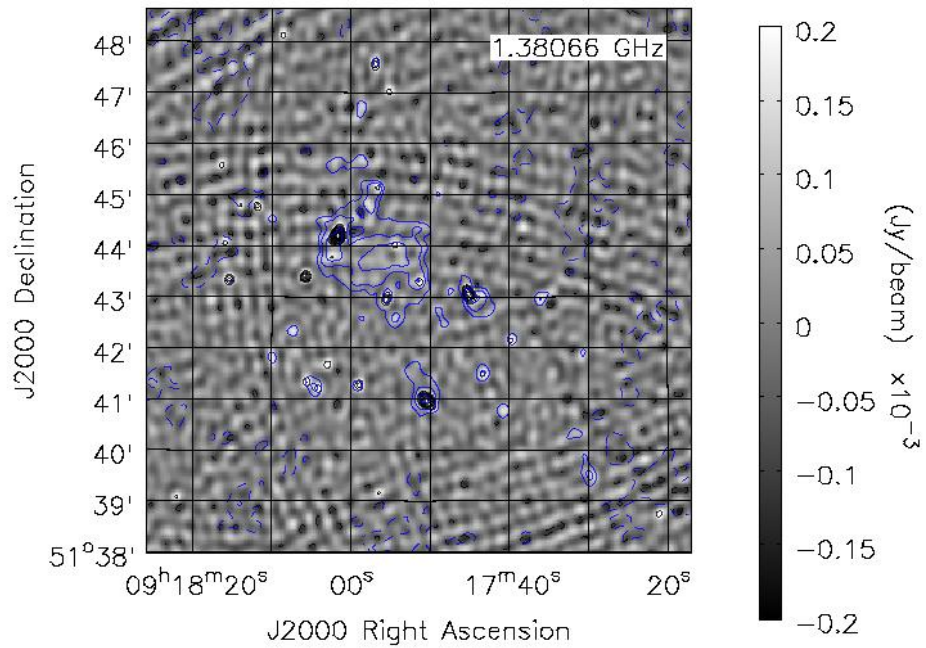
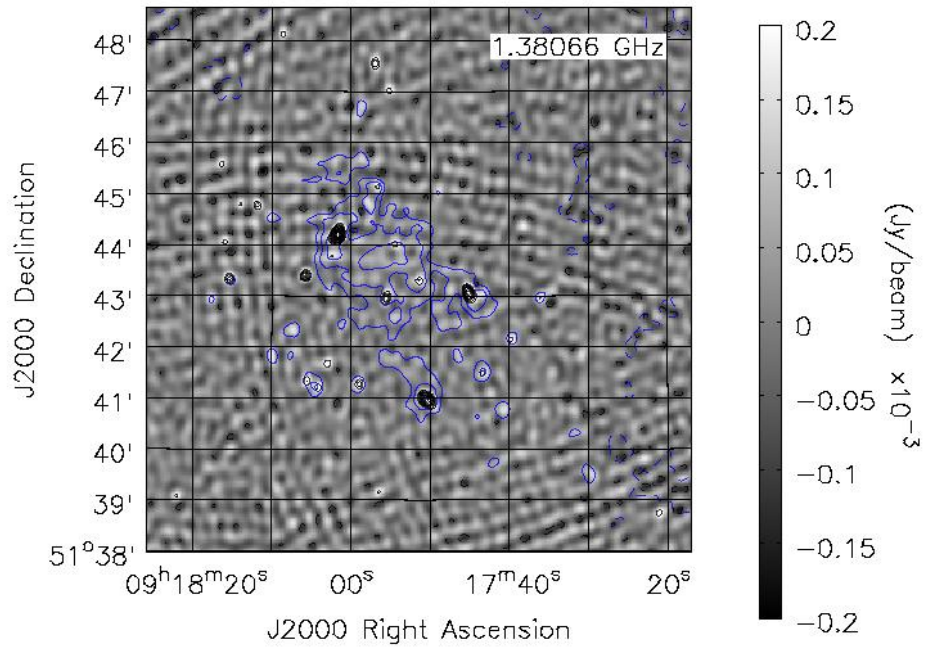


FIGURE 4.8: *Top panel:* Contours (blue) from the $r = 0.75$ image (Figure 4.7 *bottom panel*) overlaid on the uniform weighted image (Figure 4.6). Contours (blue) are drawn at $-3, 5, 7$ and $10 \times \sigma$. *Bottom panel:* Contours (blue) from the $r = 0.75$ image with baselines longer than 50 m overlaid on the uniform weighted image (Figure 4.6). Contours (blue) are drawn at $-3, 5, 7$ and $10 \times \sigma$.

Chapter 5

Observations of Abell 773 at 19.43 cm

5.1 Observations and data reduction at 19.43 cm

In this chapter, we jointly image the 18 cm and 21 cm observations with the goal to further suppress sidelobe contamination and artefacts through multi frequency synthesis. Using the calibrated datasets from Chapters 3 and 4, the uniform weighted image shown in Figure 5.1 was created using the Cotton-Schwab CLEAN algorithm (Cornwell et al., 1999) by deconvolving down to a flux density threshold of 3σ , where σ is the final image noise of $0.022 \text{ mJy beam}^{-1}$. The reference frequency is now 1.544 GHz corresponding to $\lambda = 19.43 \text{ cm}$. The image has a synthesized beam size of $12'' \times 9''$ and a $0.022 \text{ mJy beam}^{-1}$ noise. In comparison, the 1.380 GHz radio image in Figure 4.5 has a $14'' \times 11''$ synthesized beam and a $0.03 \text{ mJy beam}^{-1}$ noise. A visual inspection of the centre of A 773 (Figure 5.1) shows a significant reduction of artefacts present at the centre of the radio image.

To assess the impact of combining the two frequencies on the presence of diffuse radio emission at the cluster centre, we first proceeded to re-image the residual visibility data at 18 cm and 21 cm after the compact sky model was subtracted. Since the radio images obtained with robust parameter $r = 0.75$ at 18 cm and 21 cm were considered to have the best brightness sensitivity, we adopted the same Briggs weighting for the joint residuals visibility data. Figure 5.2 (*Top panel*) shows contours (blue) of the diffuse radio emission overlaid on the uniform weighted image. The diffuse emission is more extended with a linear size of $\sim 4 \text{ arcmin}$, corresponding to an area of 6.75 arcmin^2 (~ 68 synthesized beams) and a 5σ integrated flux density of 10.2 mJy .

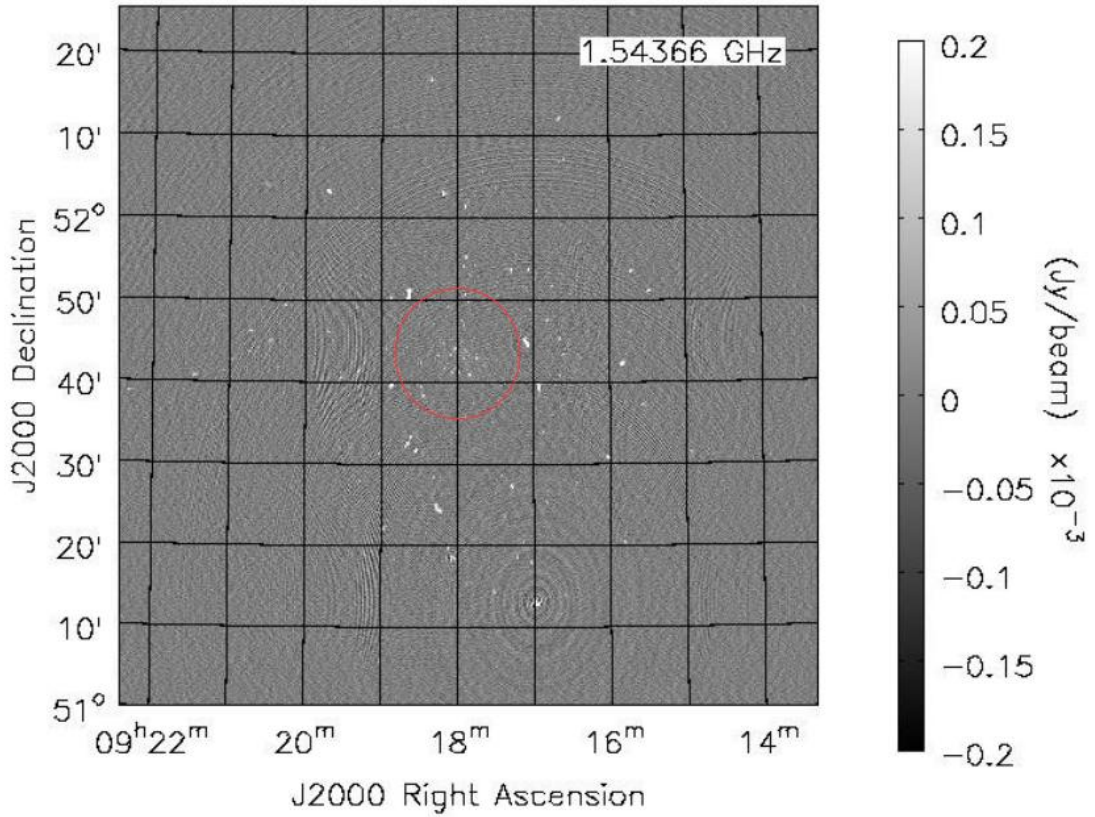


FIGURE 5.1: Uniform weighted image of A 773 at 19.43 cm. The angular resolution is $12'' \times 9''$ and the noise level $0.022 \text{ mJy beam}^{-1}$. The contamination at the centre of the field due to secondary sidelobes originating from the bright off-axis radio source in the south of the image appears to be partially suppressed.

As it was done in the analysis of 18 cm and 21 cm data, we filtered out the largest-scale emission by excluding baselines shorter than 50 m. Figures 5.2 (*Top panel*) and 5.2 (*Bottom panel*) show that the shape of the diffuse radio emission becomes more regular but less extended with the 50 m baseline cut compared to the image with no baseline cut. The linear size of the radio halo is now ~ 3.9 arcmin, corresponding to a 5.4 arcmin^2 area, with a 5σ integrated flux density of 6.76 mJy. While the linear extent of the radio halo remained essentially the same after excluding baselines shorter than 50 m from the image, its area decreased by $\sim 20\%$ and its flux density by $\sim 34\%$, showing that significant power is present in the very short baselines, although it is not clear which fraction of this power is due to Galactic emission and which fraction to the radio halo.

A comparison between Figures 4.8 (*Bottom panel*) and 5.2 (*Bottom panel*) shows that the noise in the 1.544 GHz radio image is $\sim 30\%$ reduced with a 14% decrease in the synthesized beam. The radio halo in the 1.544 GHz radio image appears more extended

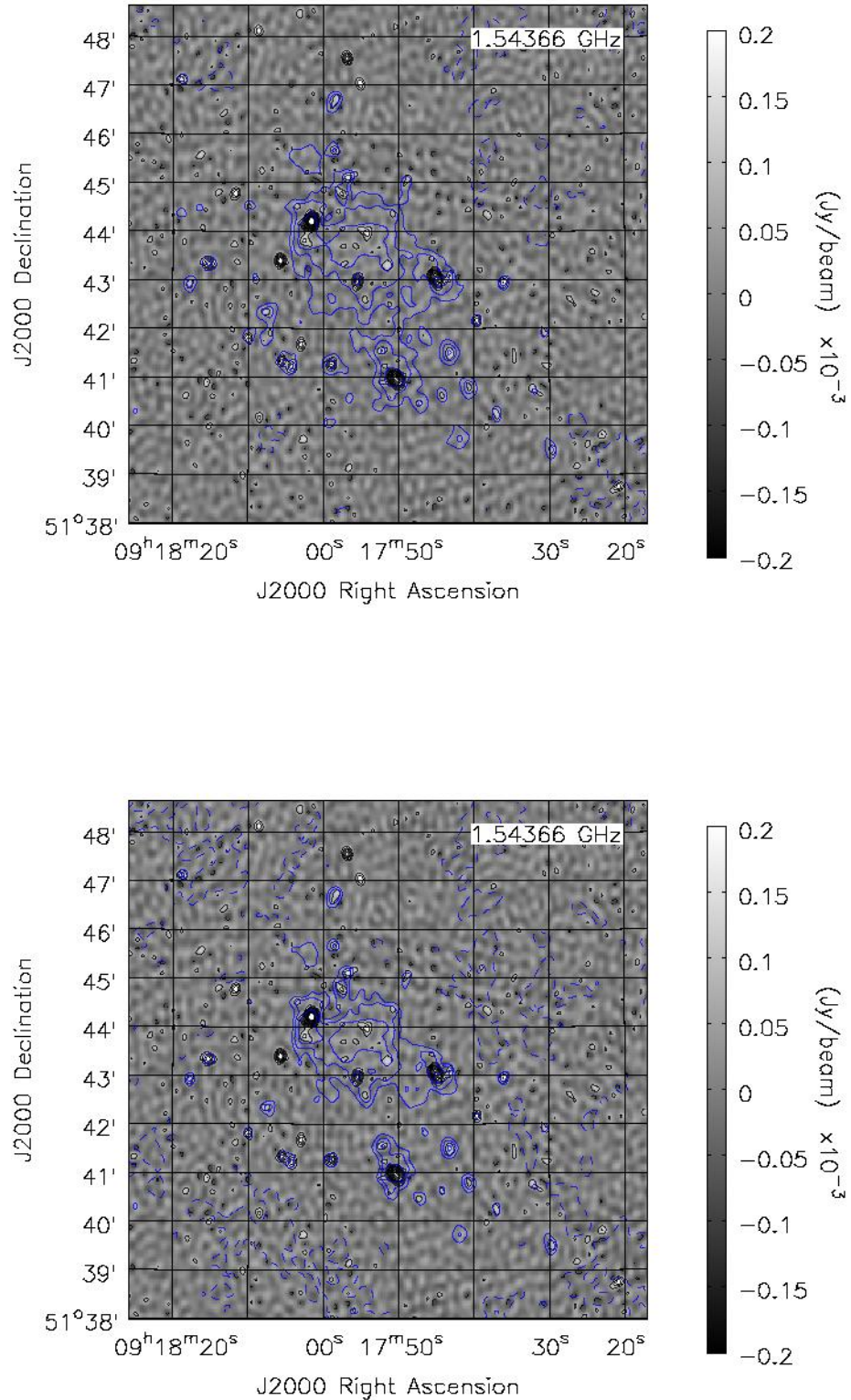


FIGURE 5.2: *Top panel*: Contours (blue) from the residual $r = 0.75$ image overlaid on the uniform weighted (Figure 5.1, black contours) image. The angular resolution and noise rms are $21'' \times 17''$ and $0.021 \text{ mJy beam}^{-1}$ respectively. The contours (blue) are drawn at $5, 7$ and 10σ . *Bottom panel*: Same as Figure 5.2 (*Top panel*) but excluding the baselines shorter than 50 m for the residual $r = 0.75$ image. The angular resolution and noise rms are $21'' \times 17''$ and $0.017 \text{ mJy beam}^{-1}$ respectively.

and brighter than in the individual images. Overall, artefacts in the 1.544 GHz image are partially suppressed, providing further significance for the presence of a radio halo.

Chapter 6

Conclusion

In this thesis, we have presented 18 cm and 21 cm observations of the A 773 galaxy cluster observed with the Westerbork radio telescope.

The 18 cm and 21 cm datasets were individually reduced and imaged. In both cases we used images at the highest resolution (uniformly weighted) to identify a sky model composed of compact radio sources. The uniform weighted images achieved a noise level of $0.03 \text{ mJy beam}^{-1}$ at 18 cm and 21 cm. The compact source sky model was then subtracted from the data at both frequencies to form residual visibilities that were imaged at lower resolution.

Diffuse emission at the cluster centre was identified in the 18 cm images with a $19'' \times 15''$ angular resolution and noise of $0.02 \text{ mJy beam}^{-1}$. The 18 cm images may be affected by confusion due to Galactic emission and we attempted to filter out the Galactic contribution by excluding the baselines shorter than 50 m from the image. In this way the candidate radio halo with an area of 2.65 arcmin^2 (or 0.44 Mpc in size) and a 3.62 mJy flux density.

The 21 cm images were obtained following the same procedure but were, unfortunately, affected by secondary sidelobe contamination from a few bright sources away from the pointing direction. These sources could be removed through a direction dependent calibration that we did not, however, attempt in this thesis. Nevertheless, also at 21 cm we found evidence of a radio halo, however, with morphology a bit different than at 18 cm.

In order to provide further, convincing evidence of the presence and morphology of the radio halo, we jointly imaged the 18 cm and 21 cm datasets obtaining a final image at the reference frequency of 1.544 GHz. Also in this case, residual visibilities were formed by subtracting the compact source sky model and were imaged at lower resolution. We

obtained a suppression of the artefacts that affected the 21 cm image, enabling a clearer analysis of the halo properties. In the combined 19.43 cm image, the radio halo has a 6.75 arcmin^2 area with a 10.2 mJy flux density. Like in the 18 cm case, we attempted to filter out the Galactic contribution by excluding the baselines shorter than 50 m from the image. In this way, we obtain a radio halo with a 5.37 arcmin^2 (or 0.62 Mpc in size at $z = 0.217$) area with a 6.76 mJy flux density. Compared to the detection presented in [Govoni et al. \(2001\)](#), the two morphologies are in fair qualitative agreement, although the radio halo is $\sim 50\%$ fainter in our observations.

Given the uncertainty on the presence of a radio halo in our data, we could not carry out any reliable spectral index measurement, which is left for future work.

Bibliography

- Ackermann M., Ajello M., Albert A., Allafort A., Atwood W., Baldini L., Ballet J., Barbiellini G., Bastieri D., Bechtol K., et al., 2014, *The Astrophysical Journal*, 787, 18
- Ade P. A., Aghanim N., Arnaud M., Ashdown M., Aumont J., Baccigalupi C., Balbi A., Banday A., Barreiro R., Bartelmann M., et al., 2011, *Astronomy & Astrophysics*, 536, A8
- Aharonian F., Akhperjanian A., Anton G., De Almeida U. B., Bazer-Bachi A., Becherini Y., Behera B., Bernlöhr K., Boisson C., Bochow A., et al., 2009, *Astronomy & Astrophysics*, 502, 437
- Ahnen M. L., Ansoldi S., Antonelli L., Antoranz P., Babic A., Banerjee B., Bangale P., De Almeida U. B., Barrio J., González J. B., et al., 2016, *Astronomy & Astrophysics*, 589, A33
- Aleksić J., Alvarez E., Antonelli L., Antoranz P., Asensio M., Backes M., de Almeida U. B., Barrio J., Bastieri D., González J. B., et al., 2012, *Astronomy & Astrophysics*, 541, A99
- Aleksić J., Antonelli L., Antoranz P., Backes M., Baixeras C., Balestra S., Barrio J., Bastieri D., González J. B., Bednarek W., et al., 2010, *The Astrophysical Journal*, 710, 634
- Anderson B., Zimmer S., Conrad J., Gustafsson M., Sánchez-Conde M., Caputo R., 2016, *Journal of Cosmology and Astroparticle Physics*, 2016, 026
- Atwood W., Abdo A. A., Ackermann M., Althouse W., Anderson B., Axelsson M., Baldini L., Ballet J., Band D., Barbiellini G., et al., 2009, *The Astrophysical Journal*, 697, 1071
- Bagchi J., Sirothia S., Werner N., Pandge M. B., Kantharia N. G., Ishwara-Chandra C., Paul S., Joshi S., et al., 2011, *The Astrophysical Journal Letters*, 736, L8
- Bahcall N. A., 1996, arXiv preprint astro-ph/9611148

- Basu K., 2012, *Monthly Notices of the Royal Astronomical Society: Letters*, 421, L112
- Beresnyak A., Xu H., Li H., Schlickeiser R., 2013, *The Astrophysical Journal*, 771, 131
- Bernardi G., de Bruyn A., Brentjens M., Ciardi B., Harker G., Jelić V., Koopmans L., Labropoulos P., Offringa A., Pandey V., et al., 2009, *Astronomy & Astrophysics*, 500, 965
- Bernardi G., Venturi T., Cassano R., Dallacasa D., Brunetti G., Cuciti V., Johnston-Hollitt M., Oozeer N., Parekh V., Smirnov O., 2015, *Monthly Notices of the Royal Astronomical Society*, 456, 1259
- Bhatnagar S., Cornwell T., Golap K., Uson J. M., 2008, *Astronomy & Astrophysics*, 487, 419
- Birkinshaw M., 1999, *Physics Reports*, 310, 97
- Blasi P., Colafrancesco S., 1999, *Astroparticle Physics*, 12, 169
- Blasi P., Gabici S., Brunetti G., 2007, *International Journal of Modern Physics A*, 22, 681
- Blumenthal G. R., Faber S., Primack J. R., Rees M. J., 1984, *Nature*, 311, 517
- Bonafede A., Brügger M., van Weeren R., Vazza F., Giovannini G., Ebeling H., Edge A., Hoeft M., Klein U., 2012, *Monthly Notices of the Royal Astronomical Society*, 426, 40
- Bonafede A., Feretti L., Murgia M., Govoni F., Giovannini G., Dallacasa D., Dolag K., Taylor G., 2010, *Astronomy & Astrophysics*, 513, A30
- Bonafede A., Intema H., Brügger M., Vazza F., Basu K., Sommer M., Ebeling H., De Gasperin F., Röttgering H., van Weeren R., et al., 2015, *Monthly Notices of the Royal Astronomical Society*, 454, 3391
- Botteon A., Shimwell T., Bonafede A., Dallacasa D., Brunetti G., Mandal S., van Weeren R., Brügger M., Cassano R., de Gasperin F., et al., 2018, *Monthly Notices of the Royal Astronomical Society*, 478, 885
- Briggs D., 1995, PhD thesis, New Mexico Institute of Mining and Technology
- Brügger M., Rafferty D., Bonafede A., van Weeren R., Shimwell T., Intema H., Röttgering H., Brunetti G., Di Gennaro G., Savini F., et al., 2018, *Monthly Notices of the Royal Astronomical Society*, 477, 3461
- Brunetti G., Blasi P., 2005, *Monthly Notices of the Royal Astronomical Society*, 363, 1173

- Brunetti G., Blasi P., Reimer O., Rudnick L., Bonafede A., Brown S., 2012, *Monthly Notices of the Royal Astronomical Society*, 426, 956
- Brunetti G., Cassano R., Dolag K., Setti G., 2009, *Astronomy & Astrophysics*, 507, 661
- Brunetti G., Jones T. W., 2014, *International Journal of Modern Physics D*, 23, 1430007
- Brunetti G., Lazarian A., 2010, *Monthly Notices of the Royal Astronomical Society*, 410, 127
- Brunetti G., Lazarian A., 2011, *Monthly Notices of the Royal Astronomical Society*, 412, 817
- Brunetti G., Lazarian A., 2016, *Monthly Notices of the Royal Astronomical Society*, 458, 2584
- Brunetti G., Setti G., Feretti L., Giovannini G., 2001, *Monthly Notices of the Royal Astronomical Society*, 320, 365
- Brunetti G., Zimmer S., Zandanel F., 2017, *Monthly Notices of the Royal Astronomical Society*, 472, 1506
- Bykov A., Dolag K., Durret F., 2008, in , *Clusters of Galaxies*. Springer, pp 119–140
- Cassano R., Brunetti G., Venturi T., Setti G., Dallacasa D., Giacintucci S., Bardelli S., 2008, *Astronomy & Astrophysics*, 480, 687
- Cassano R., Etori S., Brunetti G., Giacintucci S., Pratt G., Venturi T., Kale R., Dolag K., Markevitch M., 2013, *The Astrophysical Journal*, 777, 141
- Cassano R., Gitti M., Brunetti G., 2008, *Astronomy & Astrophysics*, 486, L31
- Clark B., 1980, *Astronomy and Astrophysics*, 89, 377
- Cohen A., Clarke T. E., 2011, arXiv preprint arXiv:1102.4606
- Condon J. J., Cotton W., Greisen E., Yin Q., Perley R., Taylor G., Broderick J., 1998, *The Astronomical Journal*, 115, 1693
- Condon J. J., Ransom S. M., 2016, *Essential radio astronomy*. Vol. 2, Princeton University Press
- Cornwell T., Braun R., Briggs D. S., 1999, in *Synthesis Imaging in Radio Astronomy II* Vol. 180, Deconvolution. p. 151
- Cornwell T., Perley R., 1992, *Astronomy and Astrophysics*, 261, 353

- Cuciti V., Brunetti G., van Weeren R., Bonafede A., Dallacasa D., Cassano R., Venturi T., Kale R., 2018, *Astronomy & Astrophysics*, 609, A61
- de Gasperin F., Intema H., van Weeren R., Dawson W., Golovich N., Wittman D., Bonafede A., Brüggen M., 2015, *Monthly Notices of the Royal Astronomical Society*, 453, 3483
- de Gasperin F., Intema H. T., Shimwell T. W., Brunetti G., Brüggen M., Enßlin T. A., van Weeren R. J., Bonafede A., Röttgering H. J., 2017, *Science advances*, 3, e1701634
- de Gasperin F., Ogorean G., van Weeren R., Dawson W., Brüggen M., Bonafede A., Simionescu A., 2015, *Monthly Notices of the Royal Astronomical Society*, 448, 2197
- de Gasperin F., van Weeren R., Brüggen M., Vazza F., Bonafede A., Intema H., 2014, *Monthly Notices of the Royal Astronomical Society*, 444, 3130
- Dennison B., 1980, *The Astrophysical Journal*, 239, L93
- Di Gennaro G., Van Weeren R., Hoeft M., Kang H., Ryu D., Rudnick L., Forman W., Röttgering H., Brüggen M., Dawson W., et al., 2018, *The Astrophysical Journal*, 865, 24
- Donnert J., Dolag K., Brunetti G., Cassano R., 2013, *Monthly Notices of the Royal Astronomical Society*, 429, 3564
- Ekers R. D., 1984, in *Serendipitous Discoveries in Radio Astronomy The almost serendipitous discovery of self-calibration*. p. 154
- Enßlin T., Pfrommer C., Miniati F., Subramanian K., 2011, *Astronomy & Astrophysics*, 527, A99
- Ensslin T. A., 2001, *Astronomy & Astrophysics*, 366, 26
- Ensslin T. A., Brueggen M., 2002, *Monthly Notices of the Royal Astronomical Society*, 331, 1011
- Feretti L., 2002, in *Symposium-International Astronomical Union Vol. 199, Observational properties of diffuse halos in clusters*. pp 133–140
- Feretti L., 2005, *Advances in Space Research*, 36, 729
- Feretti L., Giovannini G., 1996, in *Symposium-International Astronomical Union Vol. 175, Diffuse cluster radio sources*. pp 333–338
- Feretti L., Giovannini G., Govoni F., Murgia M., 2012, *The Astronomy and Astrophysics Review*, 20, 54

- Giacintucci S., Markevitch M., Brunetti G., ZuHone J. A., Venturi T., Mazzotta P., Bourdin H., 2014, *The Astrophysical Journal*, 795, 73
- Giacintucci S., Markevitch M., Cassano R., Venturi T., Clarke T. E., Brunetti G., 2017, *The Astrophysical Journal*, 841, 71
- Giacintucci S., Markevitch M., Venturi T., Clarke T. E., Cassano R., Mazzotta P., 2013, *The Astrophysical Journal*, 781, 9
- Giovannini G., Bonafede A., Feretti L., Govoni F., Murgia M., Ferrari F., Monti G., 2009, *Astronomy & Astrophysics*, 507, 1257
- Giovannini G., Feretti L., 2000, *New Astronomy*, 5, 335
- Giovannini G., Feretti L., 2002, in , *Merging Processes in Galaxy Clusters*. Springer, pp 197–227
- Giovannini G., Feretti L., Girardi M., Govoni F., Murgia M., Vacca V., Bagchi J., 2011, *Astronomy & Astrophysics*, 530, L5
- Giovannini G., Feretti L., Stanghellini C., 1991, *Astronomy and Astrophysics*, 252, 528
- Giovannini G., Feretti L., Venturi T., Kim K.-T., Kronberg P., 1993, *The Astrophysical Journal*, 406, 399
- Giovannini G., Tordi M., Feretti L., 1999, *New Astronomy*, 4, 141
- Gitti M., Brighenti F., McNamara B. R., 2012, *Advances in Astronomy*, 2012
- Gitti M., Brunetti G., Feretti L., Setti G., 2004, *Astronomy & Astrophysics*, 417, 1
- Gitti M., Brunetti G., Setti G., 2002, *Astronomy & Astrophysics*, 386, 456
- Govoni F., Feretti L., 2004, *International Journal of Modern Physics D*, 13, 1549
- Govoni F., Feretti L., Giovannini G., Böhringer H., Reiprich T., Murgia M., 2001, *Astronomy & Astrophysics*, 376, 803
- Govoni F., Murgia M., Markevitch M., Feretti L., Giovannini G., Taylor G., Carretti E., 2009, *Astronomy & Astrophysics*, 499, 371
- Han J., Frenk C. S., Eke V. R., Gao L., White S. D., Boyarsky A., Malyshev D., Ruchayskiy O., 2012, *Monthly Notices of the Royal Astronomical Society*, 427, 1651
- Högbom J., 1974, *Astronomy and Astrophysics Supplement Series*, 15, 417
- Jarvis M. J., Taylor A., Agudo I., Allison J. R., Deane R., Frank B., Gupta N., Heywood I., Maddox N., McAlpine K., et al., 2017, arXiv preprint arXiv:1709.01901

- Kale R., Venturi T., Giacintucci S., Dallacasa D., Cassano R., Brunetti G., Cuciti V., Macario G., Athreya R., 2015, *Astronomy & Astrophysics*, 579, A92
- Kale R., Venturi T., Giacintucci S., Dallacasa D., Cassano R., Brunetti G., Macario G., Athreya R., 2013, *Astronomy & Astrophysics*, 557, A99
- Kazemi S., Yatawatta S., 2013, *Monthly Notices of the Royal Astronomical Society*, 435, 597
- Kazemi S., Yatawatta S., Zaroubi S., Lampropoulos P., De Bruyn A., Koopmans L., Noordam J., 2011, *Monthly Notices of the Royal Astronomical Society*, 414, 1656
- Kempner J. C., Blanton E. L., Clarke T. E., Enßlin T. A., Johnston-Hollitt M., Rudnick L., 2004, in *The riddle of cooling flows in galaxies and clusters of galaxies Conference note: a taxonomy of extended radio sources in clusters of galaxies*
- Keshet U., Loeb A., 2010, *The Astrophysical Journal*, 722, 737
- Knowles K., Baker A., Basu K., Bharadwaj V., Deane R., Devlin M., Dicker S., de Gasperin F., Ferrari C., Hilton M., et al., 2017, arXiv preprint arXiv:1709.03318
- Liang H., Hunstead R., Birkinshaw M., Andreani P., 2000, *The Astrophysical Journal*, 544, 686
- Liang Y.-F., Shen Z.-Q., Li X., Fan Y.-Z., Huang X., Lei S.-J., Feng L., Liang E.-W., Chang J., 2016, *Physical Review D*, 93, 103525
- Lindner R. R., Baker A. J., Hughes J. P., Battaglia N., Gupta N., Knowles K., Marriage T. A., Menanteau F., Moodley K., Reese E. D., et al., 2014, *The Astrophysical Journal*, 786, 49
- Loi F., Murgia M., Govoni F., Vacca V., Feretti L., Giovannini G., Carretti E., Gastaldello F., Girardi M., Vazza F., et al., 2017, *Monthly Notices of the Royal Astronomical Society*, 472, 3605
- McMullin J., Waters B., Schiebel D., Young W., Golap K., 2007, *RA Shaw, F. Hill, & DJ Bell (San Francisco, CA: ASP)*, 127
- Mandal S., Intema H., Shimwell T., van Weeren R., Botteon A., Röttgering H., Hoang D., Brunetti G., de Gasperin F., Giacintucci S., et al., 2019, *Astronomy & Astrophysics*, 622, A22
- Martins B. J., Rau U., 2016, in *2016 Radio Frequency Interference (RFI) Automated tuning of rfi identification and flagging algorithms*. pp 59–64
- Mazzotta P., Giacintucci S., 2008, *The Astrophysical Journal Letters*, 675, L9

- Millenaar R. P., Oosterloo T., Brentjens M., 2008, in Proc. URSI General Assembly The radio observatory at astron: News from the wsrt and lofar
- Morganti R., 2004, Technical report, The WSRT guide to observation. Tech. rep., AS-TRON
- Motl P. M., Hallman E. J., Burns J. O., Norman M. L., 2005, *The Astrophysical Journal Letters*, 623, L63
- Noordam J. E., 2004, in *Ground-Based Telescopes Vol. 5489*, Lofar calibration challenges. pp 817–825
- Noordam J. E., Smirnov O. M., 2010, *Astronomy & Astrophysics*, 524, A61
- Oozeer N., Bietenholz M., Goedhart S.,
- Pearson T., Readhead A., 1984, *Annual review of astronomy and astrophysics*, 22, 97
- Perley R. A., Butler B. J., 2017, *The Astrophysical Journal Supplement Series*, 230, 7
- Petrosian V., 2001, *The Astrophysical Journal*, 557, 560
- Pfrommer C., Ensslin T. A., 2004a, *Astronomy & Astrophysics*, 413, 17
- Pfrommer C., Ensslin T. A., 2004b, *Monthly Notices of the Royal Astronomical Society*, 352, 76
- Pfrommer C., Enßlin T. A., Springel V., 2008, *Monthly Notices of the Royal Astronomical Society*, 385, 1211
- Prokhorov D., Churazov E., 2014, *Astronomy & Astrophysics*, 567, A93
- Rajpurohit K., Hoeft M., Van Weeren R., Rudnick L., Röttgering H., Forman W., Brüggem M., Croston J., Andrade-Santos F., Dawson W., et al., 2018, *The Astrophysical Journal*, 852, 65
- Reimer O., Sreekumar P., 2004, *New Astronomy Reviews*, 48, 481
- Röttgering H., Wieringa M., Hunstead R., Ekers R., 1997, *Monthly Notices of the Royal Astronomical Society*, 290, 577
- Ruhl J., Ade P. A., Carlstrom J. E., Cho H.-M., Crawford T., Dobbs M., Greer C. H., Holzappel W. L., Lanting T. M., Lee A. T., et al., 2004, in *Millimeter and Submillimeter Detectors for Astronomy II Vol. 5498*, The south pole telescope. pp 11–29
- Russell H., van Weeren R., Edge A., McNamara B., Sanders J., Fabian A., Baum S., Canning R., Donahue M., O’Dea C., 2011, *Monthly Notices of the Royal Astronomical Society: Letters*, 417, L1

- Salvini S., Wijnholds S. J., 2014, *Astronomy & Astrophysics*, 571, A97
- Santos M. G., Cluver M., Hilton M., Jarvis M., Jozsa G. I., Leeuw L., Smirnov O., Taylor R., Abdalla F., Afonso J., et al., 2017, arXiv preprint arXiv:1709.06099
- Sarazin C. L., 1986, *Reviews of Modern Physics*, 58, 1
- Sarazin C. L., 2002, in , *Merging Processes in Galaxy Clusters*. Springer, pp 1–38
- Sault R., Wieringa M., 1994, *Astronomy and Astrophysics Supplement Series*, 108, 585
- Schwab F., 1984, *The Astronomical Journal*, 89, 1076
- Shimwell T., Luckin J., Brügger M., Brunetti G., Intema H., Owers M., Röttgering H., Stroe A., Van Weeren R., Williams W., et al., 2016, *Monthly Notices of the Royal Astronomical Society*, 459, 277
- Shimwell T. W., Markevitch M., Brown S., Feretti L., Gaensler B., Johnston-Hollitt M., Lage C., Srinivasan R., 2015, *Monthly Notices of the Royal Astronomical Society*, 449, 1486
- Sijbring L. G., 1993
- Slee O., Roy A., Murgia M., Andernach H., Ehle M., 2001, *The Astronomical Journal*, 122, 1172
- Smirnov O. M., 2011, *Astronomy & Astrophysics*, 527, A107
- Sommer M. W., Basu K., 2013, *Monthly Notices of the Royal Astronomical Society*, 437, 2163
- Sommer M. W., Basu K., Intema H., Pacaud F., Bonafede A., Babul A., Bertoldi F., 2016, *Monthly Notices of the Royal Astronomical Society*, 466, 996
- Sunyaev R., Zel'Dovich Y. B., 1980, *Annual review of astronomy and astrophysics*, 18, 537
- Thompson A. R., Moran J. M., Swenson G. W., et al., 2017, *Interferometry and synthesis in radio astronomy*. Springer
- Van Weeren R., Brügger M., Röttgering H., Hoeft M., Nuza S., Intema H., 2011, *Astronomy & Astrophysics*, 533, A35
- Van Weeren R., Brunetti G., Brügger M., Andrade-Santos F., Ogrean G., Williams W., Röttgering H., Dawson W., Forman W., De Gasperin F., et al., 2016, *The Astrophysical Journal*, 818, 204

- van Weeren R., de Gasperin F., Akamatsu H., Brügger M., Feretti L., Kang H., Stroe A., Zandanel F., 2019, *Space Science Reviews*, 215, 16
- Van Weeren R., Fogarty K., Jones C., Forman W., Clarke T., Brügger M., Kraft R., Lal D., Murray S., Röttgering H., 2013, *The Astrophysical Journal*, 769, 101
- van Weeren R., Hoeft M., Röttgering H., Brügger M., Intema H., van Velzen S., 2011, *Astronomy & Astrophysics*, 528, A38
- van Weeren R., Röttgering H., Brügger M., 2011, *Astronomy & Astrophysics*, 527, A114
- Venturi T., Giacintucci S., Cassano R., Brunetti G., Dallacasa D., Macario G., Setti G., Bardelli S., Athreya R., 2009, arXiv preprint arXiv:0903.2934
- Venturi T., Giacintucci S., Dallacasa D., Cassano R., Brunetti G., Bardelli S., Setti G., 2008, *Astronomy & Astrophysics*, 484, 327
- Venturi T., Rossetti M., Brunetti G., Farnsworth D., Gastaldello F., Giacintucci S., Lal D., Rudnick L., Shimwell T., Eckert D., et al., 2017, *Astronomy & Astrophysics*, 603, A125
- Wik D. R., Sarazin C. L., Ricker P. M., Randall S. W., 2008, *The Astrophysical Journal*, 680, 17
- Wilber A., Brügger M., Bonafede A., Savini F., Shimwell T., van Weeren R., Rafferty D., Mechev A., Intema H., Andrade-Santos F., et al., 2017, *Monthly Notices of the Royal Astronomical Society*, 473, 3536
- Zandanel F., Ando S., 2014, *Monthly Notices of the Royal Astronomical Society*, 440, 663
- ZuHone J., Markevitch M., Brunetti G., Giacintucci S., 2012, *The Astrophysical Journal*, 762, 78